Climatological distributions of pH, pCO_2, total CO_2, alkalinity, and $CaCO_3$ saturation in the global surface ocean, and temporal changes at selected locations

Taro Takahashi [*], S.C. Sutherland, D.W. Chipman [1], J.G. Goddard, Cheng Ho, Timothy Newberger, Colm Sweeney, D.R. Munro

Lamont-Doherty Earth Observatory of Columbia University, Palisades, NY 10964, United States
Cooperative Institute in Environmental Sciences, University of Colorado, Boulder, CO 80309, United States

ABSTRACT

Climatological mean monthly distributions of pH in the total H^+ scale, total CO_2 concentration (TCO_2), and the degree of $CaCO_3$ saturation for the global surface ocean waters (excluding coastal areas) are calculated using a data set for pCO_2, alkalinity and nutrient concentrations in surface waters (depths <50 m), which is built upon the GLODAP, CARINA and LDEO databases. The mutual consistency among these measured parameters is demonstrated using the inorganic carbon chemistry model with the dissociation constants for carbonic acid by Lueker et al. (2000) and for boric acid by Dickson (1990). Linear potential alkalinity-salinity relationships are established for 24 regions of the global ocean. The mean monthly distributions of pH and carbon chemistry parameters for the reference year 2005 are computed using the climatological mean monthly pCO_2 data adjusted to a reference year 2005 and the alkalinity estimated from the potential alkalinity-salinity relationships. The equatorial zone (4°N-4°S) of the Pacific is excluded from the analysis because of the large interannual changes associated with ENSO events. The pH thus calculated ranges from 7.9 to 8.2. Lower values are located in the upwelling regions in the tropical Pacific and in the Arabian and Bering Seas; higher values are found in the subpolar and polar waters during the spring-summer months of intense photosynthetic production. The vast areas of subtropical oceans have seasonally varying pH values ranging from 8.05 during warmer months to 8.15 during colder months. The warm tropical and subtropical waters are supersaturated by a factor of as much as 4.2 with respect to aragonite and 6.3 for calcite, whereas the cold subpolar and polar waters are supersaturated by 1.2 for aragonite and 2.0 for calcite because of the lower pH values resulting from greater TCO_2 concentrations. In the western Arctic Ocean, aragonite undersaturation is observed. The time-series data from the Bermuda (BATS), Hawaii (HOT), Canary (ESTOC) and the Drake Passage show that pH has been declining at a mean rate of about -0.02 pH per decade, and that pCO_2 has been increasing at about 19 μatm per decade tracking the atmospheric pCO_2 increase rate. This suggests that the ocean acidification is caused primarily by the uptake of atmospheric CO_2. The relative importance of the four environmental drivers (temperature, salinity, alkalinity and total CO_2 concentration) controlling the seasonal variability of carbonate chemistry at these sites is quantitatively assessed. The ocean carbon chemistry is governed sensitively by the TA/TCO_2 ratio, and the rate of change in TA is equally important for the future ocean environment as is the TCO_2 in ocean waters increases in the future.

1. Introduction

Most active biological production takes place in the sun-lit surface layer of the global ocean. This is also the layer that is being acidified by the absorption of rapidly increasing CO_2 from the atmosphere. Many biogeochemical and biochemical reactions will be influenced by the changes in ocean water pH with most notably calcifying organisms such as corals, foraminifera, pteropods and coccolithophores will be impacted directly due to the reduced degree of saturation of $CaCO_3$ in seawater (Feely et al., 2012). At several time-series stations such as BATS (Bermuda Atlantic Time series Study) (Bates et al., 1996; Bates, 2007; Bates et al., 2012), HOT (Hawaii Ocean Time-series) (Dore et al., 2003; Dore et al., 2009) and ESTOC (European Station for Time series in the Ocean Canary Islands) (Gonzalez-Davila and Santana-Casiano, 2003; González-Dávila et al., 2007; Santana-Casiano et al., 2007; González-Dávila et al., 2010), the acidification of seawater has been documented for the past decades. The present pH conditions and future acidification of the global ocean waters by the oceanic uptake of CO_2 have been reviewed by Feely et al. (2009) using a Biogeochemical Ocean General Circulation Model (BOGCM). More locally, the rapid

acidification in the California Current system has been extensively investigated by Gruber et al. (2012) and Hauri et al. (2013) using a dynamic ocean circulation model combined with multi-year observations. All of these studies indicate a significant degree of acidification in the surface ocean waters. However, although pH and its change have been measured at many study sites and during cruises using various pH sensor systems, the data are not globally comparable due to calibration problems and methodological differences associated with the pH measurements (Marion et al., 2011). Presently, the global distribution of ocean water pH is based on BOGCM (e.g. Orr et al., 2005; Doney et al., 2009; Feely et al., 2009) which include limited descriptions of marine ecosystems and community productivity, but lack land-ocean interactions. An observation-based global ocean pH distribution is desired for establishing a baseline for documenting future changes in oceanic carbonate chemistry, thus placing the study of ocean acidification on a firmer ground.

The objective of this study is to obtain the climatological mean distribution of pH and associated carbon chemistry properties in global surface ocean waters with a single unified scale for the calculated pH. These properties will be computed on the basis of the observations made for CO_2 partial pressure (pCO_2), total alkalinity (TA) and total CO_2 concentration (TCO_2) in surface waters ($Z < 50$ m). It is imperative that these observations are based on common standards which are stable over many decades to insure the compatibility of the data in space and time. In Section 2, the principles for the method employed in this study will be briefly explained. In Section 3, the potential alkalinity (PALK = TA + nitrate)-salinity relationships observed in 24 oceanic regions will be presented. The mean monthly distributions of TA and pCO_2 in surface waters of the global ocean in a grid with 4° x 5° spatial resolution, which will be used for computing pH and other carbon chemistry properties, will be shown. In Section 4, the computed results are tested against the observations made at various locations including the BATS, HOT and ESTOC sites, and the limitations of the method used for this study are discussed. In Section 5, the climatological distribution of pH, degree of $CaCO_3$ saturation and TCO_2 in the global ocean excluding the coastal areas and the equatorial Pacific zone will be presented, and in Section 6, the decadal mean rate of changes, the seasonal variability of these properties and the drivers for seasonal changes at the four time-series stations will be discussed.

2. Principles

The concentrations of H^+ (or pH) and $CO_3^=$ ions and the degree of saturation of calcite and aragonite in seawater may be computed using an inorganic equilibrium model for carbonate chemistry in seawater when temperature, salinity, pCO_2, TCO_2 or the total alkalinity are measured. The most desirable way for computing pH and carbonate chemistry parameters is to use pCO_2 and TCO_2 for the following two reasons: a) both pCO_2 and TCO_2 measurements share the well-established air-CO_2 gas mixture standards (e. g. those of Keeling, 1960 and the NOAA Earth System Research Laboratory, Boulder, CO); and b) the solubility of CO_2 and dissociation constants for carbonic acid in seawater are the only information needed. On the other hand, seasonal variability of pCO_2 and TCO_2 is large due to seasonal changes in SST, net community production and the upwelling of deep waters. While seasonal variability data for pCO_2 are available for many locations in the global oceans (e.g. Takahashi et al., 2009, 2013; Bakker et al., 2014), the TCO_2 observations are too few to define seasonal changes other than those obtained at a few time-series stations. Consequently, the TCO_2 data are not sufficient for establishing the global distribution of pH and other carbonate chemistry parameters, although the available data may be used for testing and validating the internal consistency of our analysis method.

The carbonate chemistry in seawater may be also defined using a combination of pCO_2 and the total alkalinity (TA). However, this scheme requires additional measurements for the concentrations of boric, phosphoric and silicic acids as well as the knowledge of the dissociation constants for each acid species, in order to compute the carbonate alkalinity by correcting the contribution of these acids to the TA. Thus, the errors may be larger for high nutrient waters in high latitude and upwelling areas. TA in surface water is governed primarily by a) water balance (i.e. evaporation-precipitation, or E-P), b) upwelling of high alkalinity deep waters (due to the dissolution of $CaCO_3$), c) production or decomposition of $CaCO_3$ shells and organic carbon within the mixed layer and d) mixing between waters with different characteristics. However, seasonal variability of TA is much smaller than that of TCO_2, since the vertical gradient for TA in the upper five hundred meters of the water column is much smaller (1/2 to 1/10) than that for TCO_2, and since the biological production of $CaCO_3$ shells is commonly less than 1/10 the net community production of organic carbon with the exception of the coccolithophore blooms (Balch et al., 2005). The TA values normalized to a constant salinity are found to be seasonally invariant in the low nutrient oligotrophic waters (e. g. Bates et al., 1996; Bates, 2001). On the other hand, TA in high nutrient waters, which contain up to 30 μmol kg^{-1} for NO_3^- and 2.5 μmol kg^{-1} for phosphate due to upwelling of deep waters (e. g. Takahashi et al., 1993; Hales and Takahashi, 2004), may be altered seasonally by as much as 32 μeq kg^{-1} by biological utilization. The TA values which are used for this study include the contribution of NO_3^- and as well as that of $HPO_4^=$ because the titration was terminated at a pH of about 3 (Chen et al., 1982). Although $HPO_4^=$ contributes up to 2 μeq kg^{-1} of TA in waters rich in phosphate, we use in our analysis the salinity dependence of the potential alkalinity (PALK = TA + NO_3^-, Brewer and Goldman, 1976) to approximate the effect on TA of nutrient changes induced by biological activities. The contribution of phosphate ions is important and should not be neglected for the estimation of $CaCO_3$ production (Chen et al., 1982) and for the computation of pH and other carbonate chemistry parameters. However, it may be neglected for the purpose of obtaining the distribution of TA using the PALK-salinity correlation, mainly because of low concentrations of phosphate (~10% of NO_3^-) and its proportionality with NO_3^- as explained in Section 3.2.7 using the Southern Ocean data.

Our approach for estimating TA is in contrast to the previous work by Millero et al. (1998) and Lee et al. (2006), who parameterized TA as a function of salinity and SST without including parameter(s) representing explicitly the net community production. In their formulations, SST was used as a proxy for the combined effect of complex seasonal processes including net community production, $CaCO_3$ formation and lateral/vertical mixing. In our study, the TA change caused by seasonal net community production is corrected using seasonal NO_3^- data. The results of these earlier studies will be compared with those of this study in Section 3.3.1.

In this paper, the climatological distributions of pH (in the total H^+ scale), $CO_3^=$ and other related values in a 4° x 5° grid are computed with an inorganic carbonate chemistry model using the climatological mean values for surface water pCO_2 for the reference year 2005 (an up-dated version of Takahashi et al., 2009), total alkalinity, salinity and temperature. In order to demonstrate the global integrity of the computed pH and other values, TCO_2 values which are computed from the pCO_2-TA data with the chemical model are compared with the available TCO_2 data. As shown in Section 4, the computed values are found to be consistent with the observed values, with a few exceptions attributable to the relatively coarse 4° x 5° spatial resolution used in this study. The following dissociation constants and CO_2 solubility in seawater are used in the equilibrium carbon chemistry model: Lueker et al. (2000) for carbonic acid, Dickson (1990) for boric acid, Dickson and Riley (1979a) for water, Dickson and Riley (1979b) for phosphoric acid, Sjorberg et al. (1981) for silicic acid and Weiss (1974) for the CO_2 solubility. The dissociation constants for carbonic acid by Lueker et al. (2000) are selected because (a) their experiments are conducted by measuring all four variables (pCO_2, TCO_2, alkalinity and pH) in natural seawater samples, and (b) the pCO_2 and TCO_2 are determined using the manometric standards established by Keeling (1960) and the NOAA Earth System Research Laboratory, which are also used for the field observations in this study. In this model, the total H^+ ion scale (concentrations of free H^+ plus HSO_4^- ions (Dickson, 1993)) is used, and the TA is computed based

on the definition of Dickson (1981). The effects of organic acids are not included. The degree of saturation for calcite and aragonite are computed using the apparent solubility products (Ksp') of Mucci (1983).

3. Observations and analysis

The availability of the observations needed for this study varies widely depending on parameters. While about 6 million pCO_2 data are available for the various seasons since the 1950s over the global oceans (Takahashi et al., 2013), there are only about 16,000 TCO_2 and alkalinity measurements, mostly limited to summer months since the 1980s. In only 2,205 cases, pCO_2, TCO_2 and TA have been measured in the same samples. We will first test the mutual consistency of these three properties using this limited data set and the chemical model described in Section 2. Once this is confirmed, the global distribution of pH, TCO_2 and other carbon chemistry parameters will be computed using the climatological mean monthly distribution of pCO_2 and the alkalinity estimated using the characteristic PALK-salinity relationships found in the various ocean regions. Observed TCO_2 values will be compared with the calculated values for the validation of our method.

3.1. The TA-TCO$_2$-pCO$_2$ Database

We assembled a carbon-nutrient database (named LDEO_SurCarb Chem) for the upper 50 meters of ocean water measured during the TTO, SAVE, WOCE and CARINA programs. This database is built upon the data synthesis of the GLODAP database (Key et al., 2004), and also includes the TCO_2-TA pairs from the CARINA program (Tanhua et al., 2009; Key et al., 2010) and pCO_2 and TCO_2 data from the LDEO database (publicly available at the Biological and Chemical Oceanography Data Management Office, BCO-DMO, Woods Hole Oceanographic Institution). The pCO_2 data are based on the air-CO_2 gas mixture standards certified by Pieter Tans of NOAA Earth System Research Laboratory (ESRL), and the TCO_2 data are consistent with the CO_2 reference solutions prepared by Dickson (2001), which are based on the Keeling CO_2 standards (which are also consistent with the NOAA/ESRL values). Of about 16,000 records listed in this database, about 4,800 records are from the CARINA database and 2,600 pCO_2 data points are from LDEO database. Several thousand TCO_2 measurements made by the LDEO group are already included in the GLODAP database. Of these, 2,205 sets have pCO_2, TCO_2 and TA measured in the same samples. The mutual consistency between these three parameters in this subset is tested by comparing computed values with measured values (Fig. 1). The calculated values are found to be consistent with the measured values within the measurement uncertainties respectively: the TA values computed using pCO_2 and TCO_2 as inputs are in agreement with the measured values with a root mean square deviation (RMSD) of $\pm$ 3.9 µeq kg^{-1}; the computed TCO_2 values from the pCO_2 and alkalinity data are in agreement with the measured values within $\pm$ 3.3 µmol kg^{-1}; and the computed pCO_2 values from the TCO_2 and TA data are in agreement with the measured values within $\pm$ 6.8 µatm. This demonstrates that these three properties are mutually consistent within the context of the equilibrium model, and that one property may be computed reliably when the two others are known.

3.2. Potential Alkalinity-Salinity Relationships

In this study, we use the "LDEO SurfCarbChem" database described above, and demonstrate that PALK varies linearly with salinity within respective oceanic regions. The value of TA, which is needed for the carbonate chemistry calculation, is estimated using the PALK-salinity relationship and the NO_3^- data. The PALK-salinity relationship depends primarily on the E-P of water, the formation and dissolution of $CaCO_3$ and the mixing with waters of different characteristics (including river and deep waters). Five different cases showing how the slope of the
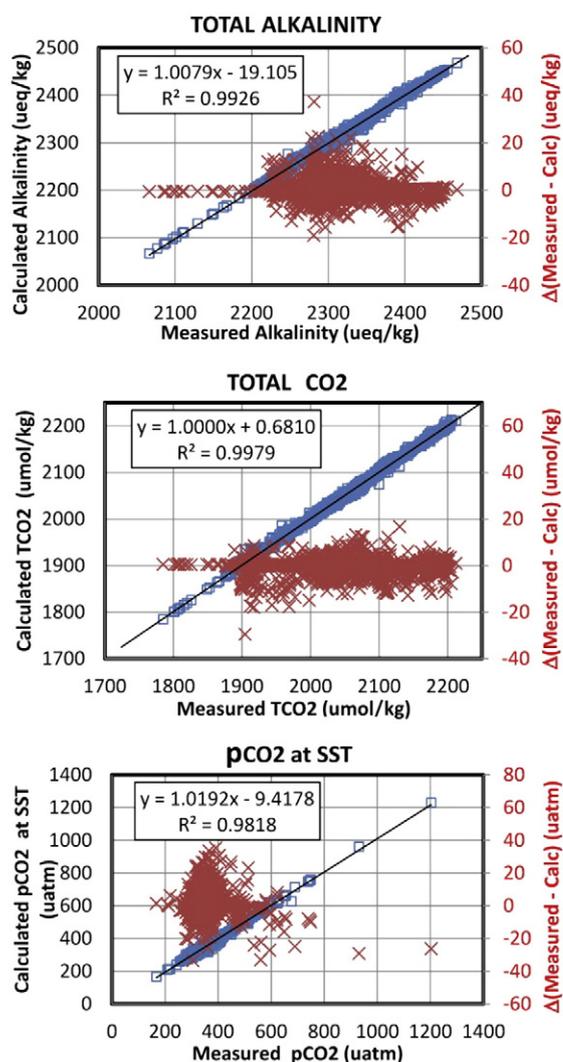
Fig. 1. Comparison of the observed values with the calculated values from the 2,205 sets of pCO_2, TCO_2 and alkalinity observations in surface waters. The black line shows the linear regression line, and the red crosses and the red right-hand axis indicate the deviations around the regression line. (Top) The calculated TA values using pCO_2 and TCO_2 are in agreement with the measured values within RMSD of $\pm$ 3.9 µeq kg^{-1}; (Middle) the calculated TCO_2 values using pCO_2 and alkalinity are in agreement with the measured values within RMSD of $\pm$ 3.3 µmol kg^{-1}; and (Bottom) the calculated pCO_2 values using TCO_2 and TA are in agreement with the measured values within $\pm$ 6.8 µatm.

linear PALK-salinity relationships varies with different oceanographic situations are illustrated in Fig. 2.

(1) The change of PALK due to the water balance (E-P) is depicted by a straight line passing through the origin and the source water (heavy open circle in Fig. 2-A and-B). An example is found in the Central Tropical North Pacific region in Fig. 5 (green line).

(2) As shown in Fig. 2-A, subtropical waters that have higher salinity and reduced PALK due to the growth of calcareous organisms (downward red arrow in the left panel) are represented by the small filled circle; in contrast, subpolar waters are less salty and enriched in PALK due to deep water upwelling (small filled circle with a upward red arrow). The mixing line between these two water types (the heavy straight line) has a gentler slope than the E-P line. Relationships of this type of relationships are commonly observed in the subtropical gyres in the Atlantic (Fig. 4), Pacific (Figs. 5 and 6) and Indian Ocean (Figs. 7 and 8), and are represented by the positive intercept values in regression lines (summarized in Table 1).

(A)

(B)
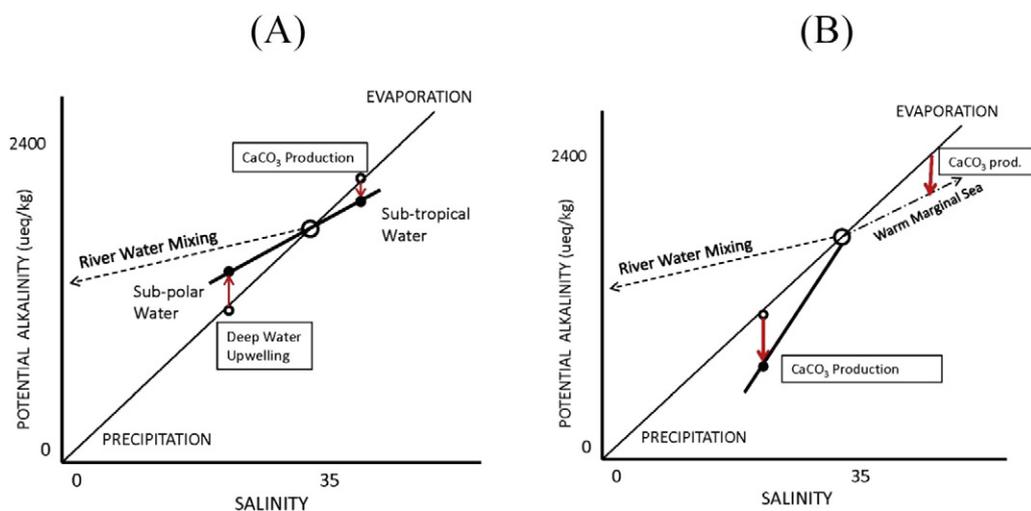
Fig. 2. Variations of the potential alkalinity-salinity relationships. The effect of evaporation and precipitation is indicated by the light solid line. The slope of the line is altered by the production/dissolution of CaCO$_3$, upwelling of deep waters, mixing with river waters, and mixing with seawaters with different compositions. See Section 3.2 for the explanation.

Table 1
The potential alkalinity-salinity relationships in 33 ocean areas. Five regions which are marked "Transition Zone", and one marked "El Niño Zone" are excluded from the analysis. The Atlantic, Indian and Pacific sectors of the Southern Ocean are combined together as a single Circumpolar Southern Ocean region (see Section 3.2.7). The remaining 24 regions are used in producing the climatological distributions of TA. PALK (μeq kg^{-1}) = (Slope) x (Salinity, PSS) + Intercept (μeq kg^{-1}), and RMSD = Root mean square deviation (μeq kg^{-1}).

	REGIONS	LOCATIONS	REGRESSION EQUATIONS			BOX AREAS
			Slope	Intercept	RMSD	
	ARCTIC & GIN SEAS					
1	West GIN Seas	66°N - 80°N, 30°W - 0°	14.12	1796.2	6.1	68 N-76 N, 332.5 to 357.5
2	East GIN Seas	66°N - 80°N, 0° - 30°E	59.57	232.0	12.3	68 N-76 N, 2.5 to 32.5
3	High Arctic	N of 80°N	27.30	1340.7	16.8	80 N-88 N, 2.5 to 357.5
4	Beaufort Sea	66°N - 80°N, 140°W - 180°	61.29	285.8	60.5	68 N-76 N, 180 to 222.5
5	Labrador Sea	55°N - 80°N, 85°W - 45°W	37.27	1016.2	17.2	56 N-76 N, 277.5 to 312.5
6	Subarctic Atlantic	55°N - 80°N, 40°W - 10°E	45.37	730.6	6.7	56 N-76 N, 317.5 to 7.5
	NORTH & SOUTH ATLANTIC OCEAN					
7	N. Atlantic Drift	40°N - 55°N, 60°W - 10°E	45.30	733.0	6.5	44 N-52 N, 302.5 to 7.5
8	Central Atlantic	40°S - 40°N, Coast to Coast	58.25	270.9	12.6	40S-40N, Ocean width
9	S. Atlantic Transition Zone	40°S - 48°S, 65°W - 30°E	30.27	1259.4	7.6	44S-48S, 297.5 to 27.5
10	S. Atlantic Subpolar Front Zone	48°S - 60°S. 70°W - 30°E	Transition Zone			48S-56S, 292.5 to 27.5
11	Antarctic (Atlantic)	60°S - 70°S, 70°W - 30°E	57.78	367.8	5.4	60S-68S, 292.5 to 27.5
	NORTH & SOUTH PACIFIC OCEAN					
12	Kuroshio-Alaska Gyre	34°N - 40°N, Ocean width				36 N , Ocean width
		& N of 40°N, E of 150°W	44.88	724.8	9.0	40 N-60 N, 107.5 to 207.5
13	N. Central Pacific	44°N - 60°N, W of 150°W	79.92	-395.7	14.7	44 N-56 N, 207.5 to 237.5
14	N. Pacific Subpolar Front Zone	40°N - 44°N, 140°E - 145°W	Transition Zone			40 N-44 N, 137.5 to 217.5
15	Okhotsk Sea	47°N - 60°N, W of 152°E	59.37	301.4	8.9	48 N-60 N, 122.5 to 152.5
16	N. Pacific Subtropical Front Zone	30°N - 34°N, 130°E - 120°W	Transition Zone			32 N, 142.5 to 242.5
17	Central Tropical N. Pacific	5°N - 30°N, W of 120°W	65.55	9.4	8.9	8 N-28 N, 107.5 to 122.5
18	Tropical East N. Pacific	5°N - 30°N, 120°W - 95°W	82.20	-553.2	9.7	8 N-28 N, 127.5 to 262.5
19	Panama Basin	0°N - 15°N, 95°W - 80°W	74.27	-290.5	8.6	8 N-12 N, 267.5 to 282.5
20	Equatorial Pacific	5°S - 5°N, 130°E - 80°W	El Nino Zone			4S-4N, 127.5 to 277.5
21	Central South Pacific	5°S - 35°S. 150°E - 84°W	66.64	-28.4	9.4	8S-36S, 142.5 to 277.5
22	E. Central South Pacific	5°S - 60°S, E of 84°W	58.88	268.5	4.0	8S-56S, 282.5 to 307.5
23	Subpolar S. Pacific	35°S - 50°S, 180° - 84°W	45.10	733.6	7.8	34S-48S, 180 to 277.5
24	S. Pacific Subpolar Front Zone	50°S - 65°S, 150°E - 70°W	Transition Zone			52S-58S, 152.5 to 297.5
25	Antarctic (Pacific)	65°S - 75°S, 140°E - 65°W	81.69	-450.8	6.7	64S-80S, 137.5 to 292.5
	NORTH & SOUTH INDIAN OCEAN					
26	Main North Indian	5°N - 25°N, 48°E - 100°E	57.07	302.3	6.7	4 N-24 N, 47.5 to 102.5
27	Red Sea	12°N - 27°N, 34°E - 48°E	26.27	1417.2	6.3	12 N-24 N, 32.5 to 47.5
28	Bengal Basin	10°N - 20°N, 80°E - 100°E	39.66	894.2	10.7	12 N-24 N, 77.5 to 102.5
29	Main South Indian	5°N - 40°S. 30°E - 140°E	65.03	20.0	7.6	4 N-36S, 27.5 to 142.5
30	S. Indian Transition	40°S - 48°S, 30°E - 175°E	23.76	1486.1	5.5	40S-48S, 27.5 to 172.5
32	S. Indian Subpolar Front Zone	48°S - 52°S, 30°E - 150°E	Transition Zone			Overlap above & below
32	Antarctic (Indian)	52°S - 70°S, 25°E - 165°E	62.57	202.0	6.6	52S-68S, 22.5 to 167.5
	SOUTHERN OCEAN					
33	Circumpolar Southern Ocean	S of 60°S, All Southern	74.13	-192.3	9.1	60S-84S, 2.5 to 357.5

(3) Fig. 2-B shows the case when PALK in lower salinity waters is reduced by growth of calcareous organisms. The mixing line for this case has a slope steeper than the E-P line. Such a case is found in the Panama Basin (Fig. 5, red line), which is represented by a negative intercept value in the regression line (Table 1).

(4) The source water may be mixed with river water that has a higher PALK value as shown by the dashed line in Fig. 2-A and -B. River waters are commonly fresh and contain PALK derived from the dissolution of limestones. This type of relationships is found in the Okhotsk Sea (black line in Fig. 5) and the Bengal Basin (red line in Fig. 7), which also have positive intercept values for regression lines (Table 1).

(5) The source water may be also mixed with waters which have high salinity and reduced PALK (marked Warm Marginal Sea in Fig. 2-B). Such a trend may be found for the mixing with an outflow from a warm evaporative basin such as the Red Sea (green line in Fig. 7).

The characteristic linear PALK-salinity relationships are observed in 27 of 33 ocean regions, and they are presented in Figs. 3 through 9. The relationships in six regions can not be described satisfactorily using linear equations because of time-space variation of complex mixing of various water types such as the subtropical-subarctic transition zones due to intense eddy mixing and the Pacific equatorial belt affected by El Niño events due to reorganization of ocean dynamics (Feely et al., 2002). These zones are indicated with the tangerine color in the sample distribution maps of Figs. 4 - 8, and are marked with special symbols in our maps. The linear regression equations and root mean square deviations (RMSD) are summarized in Table 1. Of the 33 regions listed in Table 1, five regions which are marked "Transition Zone" and one marked "El Niño Zone" are excluded from further analysis. In addition, the three Southern Ocean regions for the Atlantic, Indian and Pacific sectors are combined together as a single Circumpolar Southern Ocean region (see Section 3.2.7). The remaining 24 regions have RMSD values ranging between ± 4 and ± 17 µeq kg^{-1} with a mean RMSD of ±
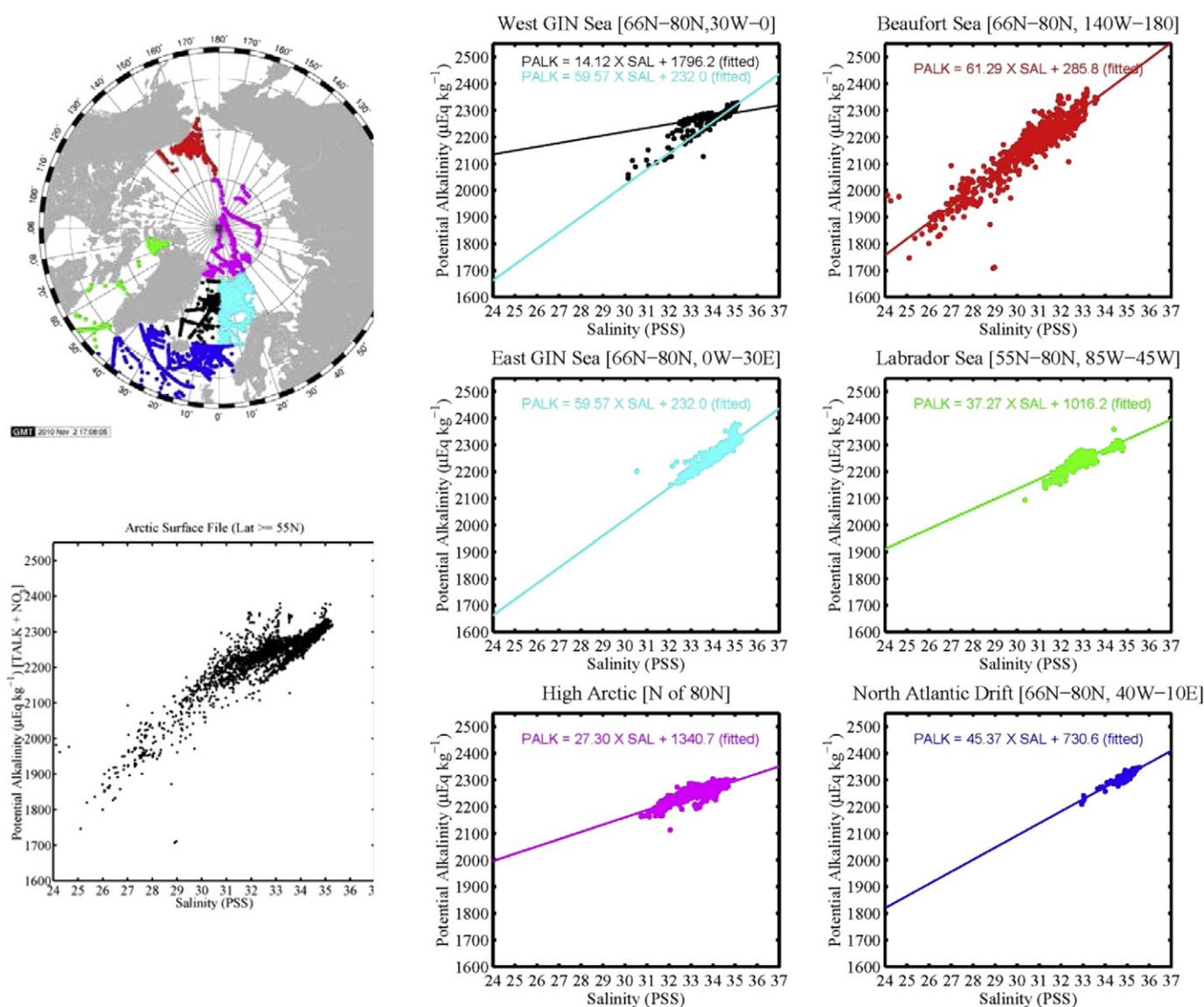
Fig. 3. Sample locations (upper left) and the potential alkalinity (PALK)-salinity relationships in the Arctic and GIN Seas. All observations are shown in the lower left plot. The data are binned into the six regions: black = Western GIN Seas (66°N-80°N, 30°W-0°), cyan = Eastern GIN Seas (66°N-80°N, 0°-30°E), magenta = high Arctic (N of 80°N), red = Beaufort Sea (66°N-80°N, 140°W-180°), green = Labrador Sea (55°N-80°N, 85°W-45°W) and blue = Subarctic Atlantic drift (66°N-80°N, 40°W-10°E). The same color code is used for the sample locations and the PALK-salinity plots (middle and right rows), in which linear regression lines and respective equations are shown. The regression equations are listed in Table 1. In the West GIN Sea plot, two lines are drawn: the cyan line is the regression line for the East GIN Sea data (shown in the plot below), and the black line is the regression line for the data excluding the points, that appear to belong to eddies from the East GIN Sea side.
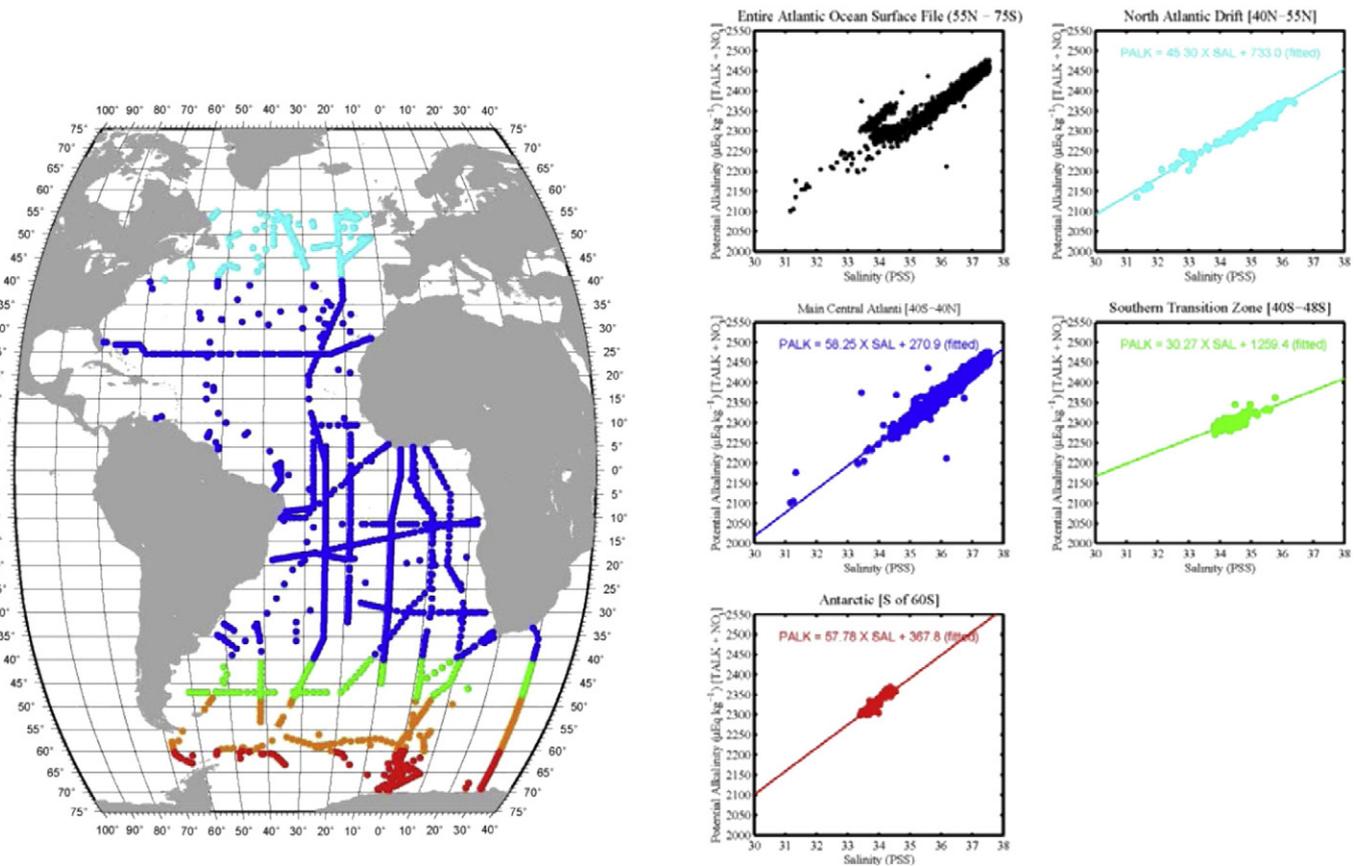
Fig. 4. Sample location map (left) and the potential alkalinity (PALK)-salinity relationships in the Atlantic. The North and South Atlantic Ocean is divided into five regions as shown in the map (left): cyan = North Atlantic drift region (40°N-55°N, 60°W-10°E), blue = main central Atlantic (40°N – 40°S), green = Southern transition zone (40°S-48°S, 60°W-30°E), tangerine = highly variable zone (48°S-60°S, 60°W-30°E) and red = Southern Ocean (60°S-70°S, 70°W-30°E). All data in the map areas are shown in the top center plot (black), and the data and the linear regression lines in four regions are shown in the plots (right) with the same color code as in the map. The regression equations are listed in Table 1. Since the data in the tangerine region are highly variable in space and time, the data and regression line in this region are not used in the analysis.

8.2 μeq kg^{-1} (excluding ± 60.5 μeq kg^{-1} for the Beaufort Sea in the Arctic, Table 1), and are used in this study. The level of deviations is considered acceptable in comparison with the precision of ± 6 μeq kg^{-1} estimated for the PALK measurements. A few regions with large RMSD will be discussed in the respective sections below.

3.2.1. Arctic-GIN Seas (north of 55°N)

Fig. 3 shows the data locations (upper left map) and the PALK data (lower left) in the Arctic and Greenland-Iceland-Norwegian (GIN) Seas. The GIN Seas are divided into two areas: the western half, which represents primarily the waters flowing out of the Arctic (including the East Greenland Current), and the eastern half, which represents the Atlantic waters flowing northward into the Arctic basin. The data and linear regression line for each of the six regions are shown in the plots on the right. The large RMSD of 60 μeq kg^{-1} in the Beaufort Sea (red plot, top right) is due to complex coastal shelf processes occurring in shallow waters comprising of the river, Arctic and Pacific sources (Anderson et al., 2004; Bates and Mathis, 2009). The high values found in the High Arctic and Labrador Sea (RMSD of 16.8 μeq kg^{-1} and 17.2 μeq kg^{-1} respectively) are also due to complex mixing of river,

ocean and ice-melt waters. Until more high-resolution measurements become available in the future, these regression lines are accepted in this study as the best representation of the available data.

3.2.2. Atlantic Ocean (55°N – 70°S)

The PALK-salinity relationships in the North and South Atlantic Ocean are shown in Fig. 4. The map on the left shows the sample locations, and black plot on the top center shows the entire data set. The North Atlantic Drift waters (40°N - 55°N) exhibit a tight linear correlation (upper right, cyan plot), and have greater PALK values than the tropical and subtropical regions by 10 to 50 μeq kg^{-1}. This may be attributed to the upwelling of deep waters as well as to the mixing of the high-alkalinity low-salinity Arctic waters. The regression line for the Drift coincides closely with that for the sub-Arctic Atlantic region (Fig. 3) as both regions are located within the subpolar gyre. The PALK distribution in the large expanse of the subtropical and tropical Atlantic Ocean between 40°N and 40°S may be characterized with a single linear regression line (blue plot) with a RMSD value of ± 12.6 μeq kg^{-1}. Although the subtropical South Atlantic waters tend to have somewhat lower PALK values, they are statistically

Fig. 5. Map (top left) shows the sample locations for the six areas in the North Pacific, where the PALK-salinity relationships are analyzed. The top right plot shows the entire data in the North Pacific (the equator-60°N), and the lower panels show the data and regression lines in the six regions: black = Okhotsk Sea, magenta = North Central-Bering Sea (44°N-60°N, 150°E-150°W), blue = Kuroshio-Alaska Gyre (34°N-40°N,135°E-150°W and 34°N-60°N, 150°W-125°W), green = Central Tropical N. Pacific (5°N-30°N, 120°W-120°E), cyan = Tropical East N. Pacific (5°N-30°N, 95°W-120°W) and red = Panama Basin (15°N-the equator, E of 95°W). The linear regression line and equation are shown in each of the six panels, and their colors coincide with the colors in the location map. The data from the tangerine areas are excluded from the analysis because of large interannual and spatial variability. The regression equations are listed in Table 1.
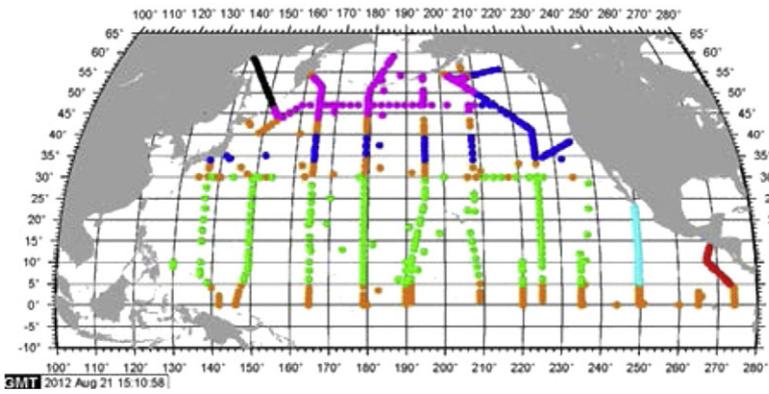
North Pacific Surface File (Eq – 60N)

Sea of Okhotsk

PALK = 59.37 X SAL + 301.4 (fitted)

North Central Pacific [44N – 60N, W of 150W]

PALK = 79.92 X SAL + –395.7 (fitted)
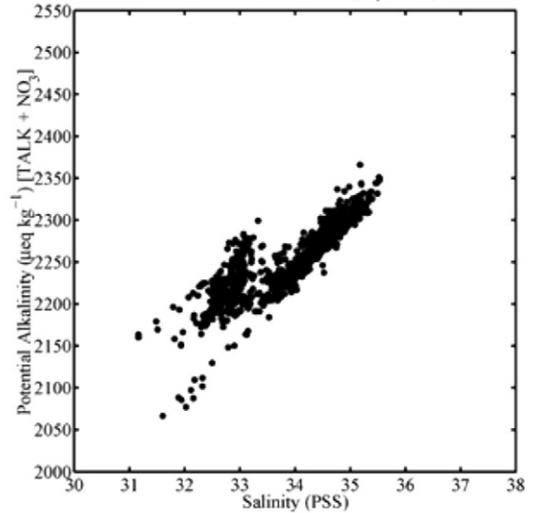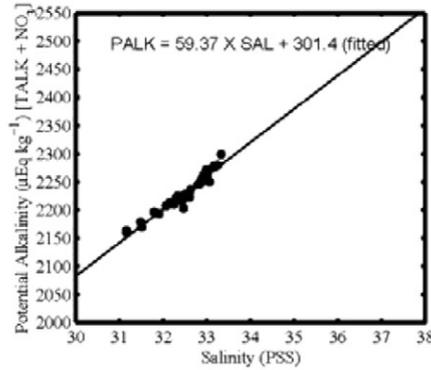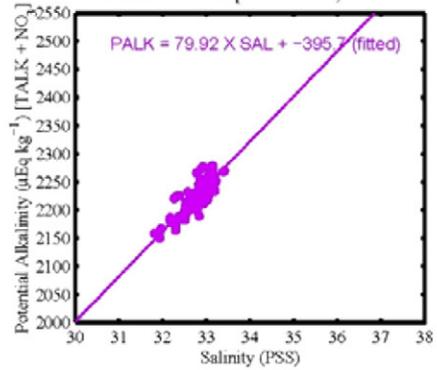
Kuroshio/Alaska Gyre [34N–40N & N of 40N & E of 150W]
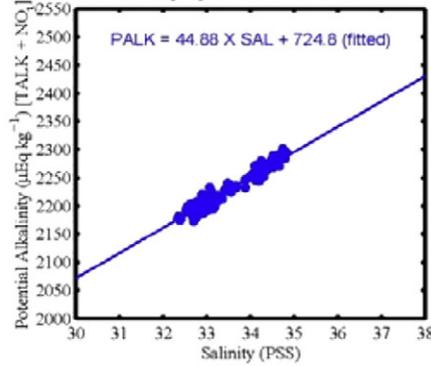
PALK = 44.88 X SAL + 724.8 (fitted)

Central Tropical N. Pacific [5N–30N, W of 120W]

PALK = 65.55 X SAL + 9.4 (fitted)

Tropical East N. Pacific [5N–30N, 95W–120W]

PALK = 82.2 X SAL + –553.2 (fitted)
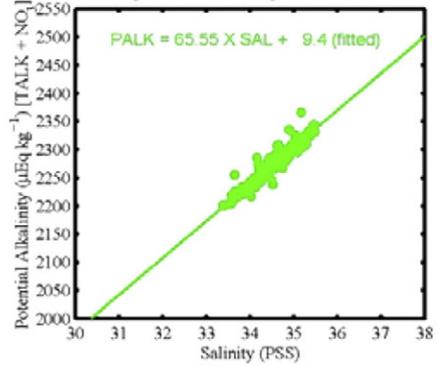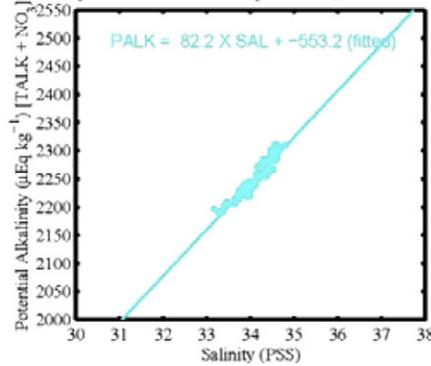
Panama Basin, [Eq–15N, E of 95W]

PALK = 74.27 X SAL + –290.5 (fitted)
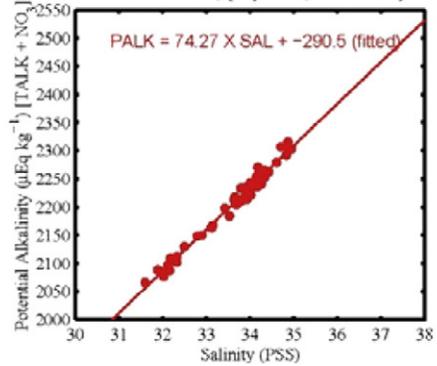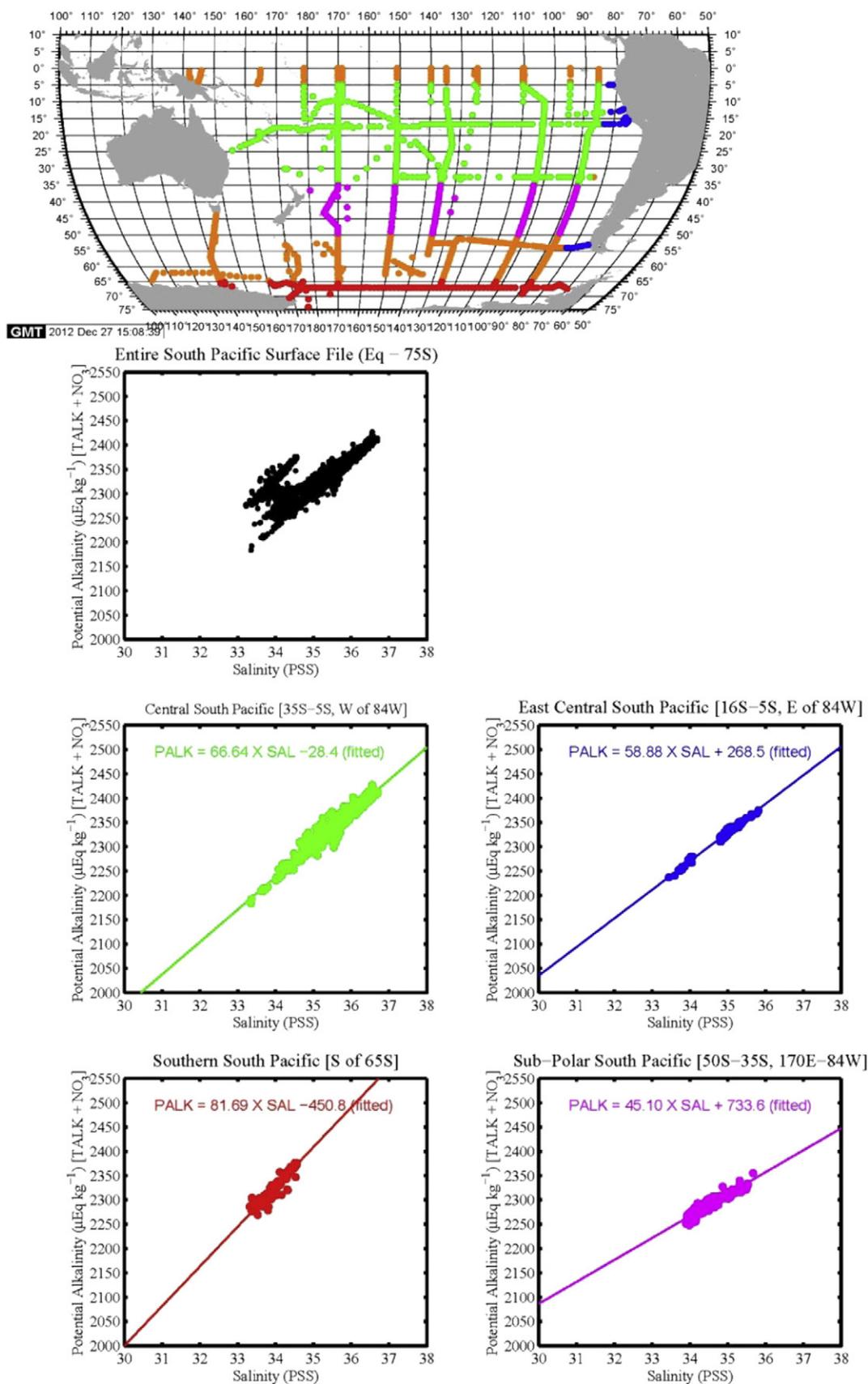
Fig. 6. Map (top center) shows the locations for the PALK-salinity data for the four areas in the South Pacific including the Southern Ocean. The top left plot (black) shows the entire data in the South Pacific (the equator-60°N), and the other panels show the data and regression lines in the four regions: green = Central South Pacific (5°S-35°S, 84°W-150°E), blue = East Central South Pacific (5°S-60°S, E of 84°W), magenta = Subpolar South Pacific (35°S-50°S, 84°W-180°), and red = Antarctic (Pacific Sector) (65°S-75°S, 65°W-140°E). The data from the tangerine areas are excluded from the analysis because of large interannual and spatial variability. The regression equations are listed in Table 1.
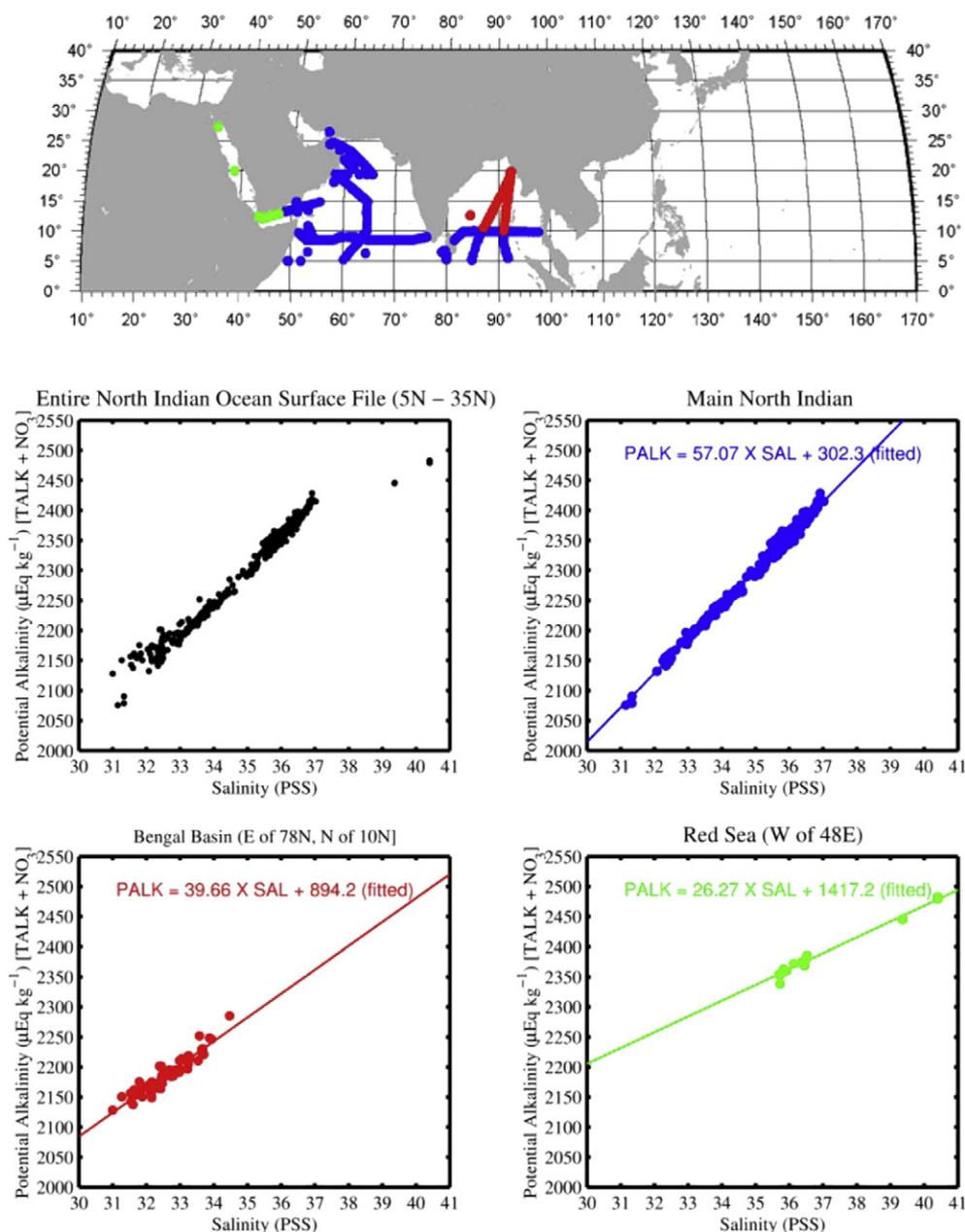
Fig. 7. Map (top center) shows the locations for the PALK-salinity data for the three areas in the North Indian Ocean (5°N – 27°N) including the Red Sea. The top left plot (black) shows the entire data in the region, and the other panels show the data and regression lines in the three areas: blue = Main North Indian Ocean (25°N (10°N)-5°N, 48°E-100°E), green = Red Sea (12°N-27°N, 34°E-48°E), and red = Bengal Basin (10°N-20°N, 80°E-100°E). Note that the salinity axis is expanded to 41 PSS because of the high salinity waters of the Red Sea. The regression equations are listed in Table 1.

indistinguishable from the northern subtropical waters. For this reason, the north and south subtropical waters are combined to yield a single regression line. In the sub-Antarctic transition zone (tangerine in the map), the PALK values vary in space and time, and no systematic trend is found. The Southern Ocean waters (red plot) have about 100 µeq kg^{-1} greater PALK than the subtropical waters. This may be also accounted for by the more intense vertical mixing in the Southern Ocean. The mean RMSD for the four regions is ± 8.0 µeq kg^{-1}.

3.2.3. North Pacific Ocean (60°N – the equator)

The six divisions in the North Pacific Ocean are shown in Fig. 5 (top left map), and the PALK-salinity relationship in the entire North Pacific is presented in the plot in the top right corner. Below them are shown colored plots for each of these six regions: the Okhotsk Sea (black), North Central-Bering Sea (magenta), Kuroshio-Alaska Gyre (blue),

Central Tropical N. Pacific (green), Tropical East N. Pacific (cyan) and Panama Basin (red). The linear regression line and equation are shown in each of the six panels, and their colors coincide with the colors in the location map in Fig. 5. The data from the tangerine areas are excluded from the analysis because of large interannual and spatial variability in the equatorial belt (i. e. El Niño) and in the northern and southern edges of the Kuroshio-North Pacific Current. The linear regression equations describing the PALK-salinity relationships in the six regions of the North Pacific are summarized in Table 1, and all of them have a mean RMSD of about ± 10 µeq kg^{-1}.

3.2.4. South Pacific Ocean (the equator-60°S)

The South Pacific (including the Pacific sector of the Southern Ocean) is divided into five regions for the PALK-salinity analysis (Fig. 6). A sub-polar region between 50°S-60°S (tangerine color) is excluded from the
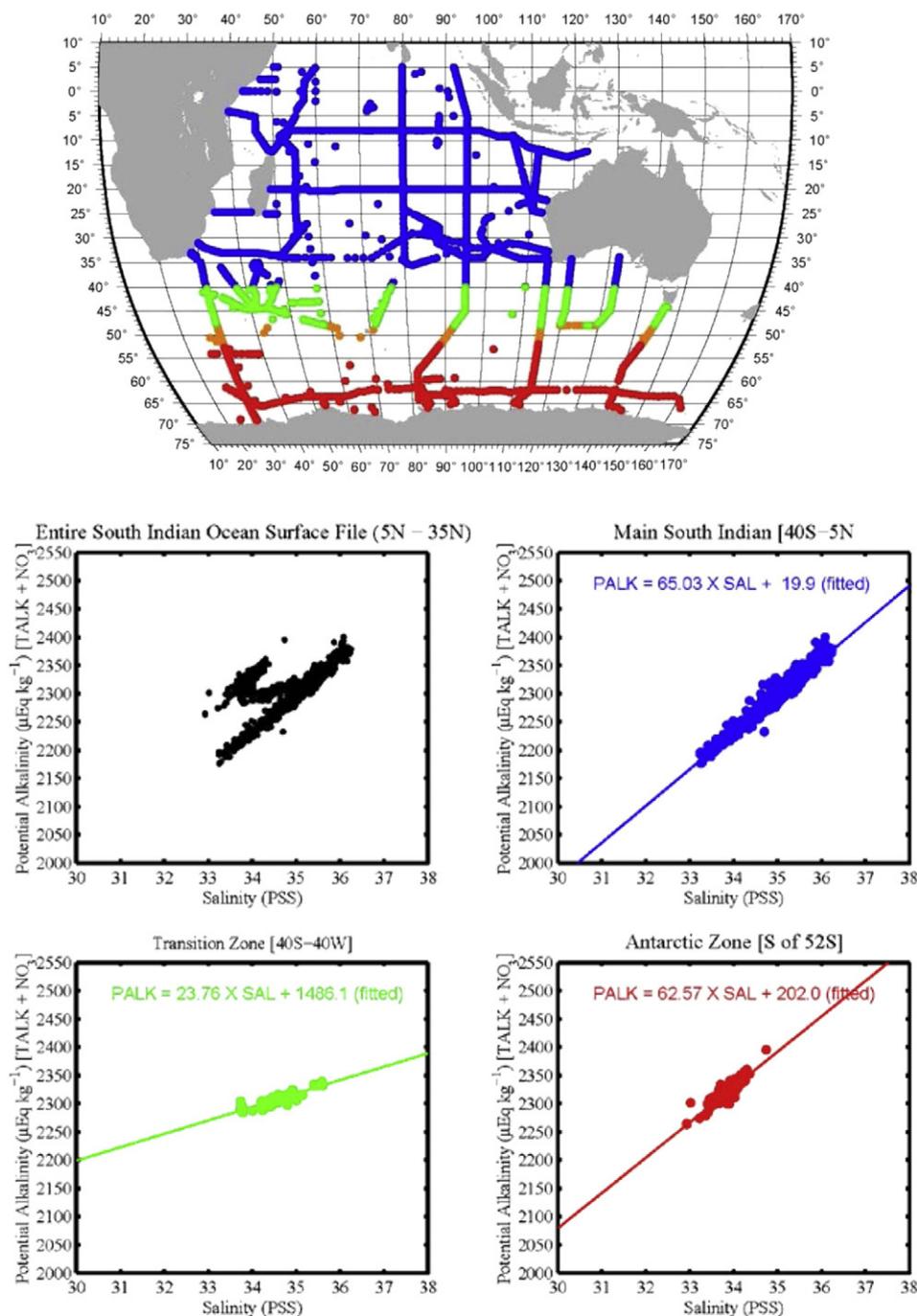
Fig. 8. Map (top center) shows the locations for the PALK-salinity data for the four regions in the South Indian Ocean (5°N – 70°S). The top left plot (black) shows the entire data in the South Indian Ocean, and the other three panels show the data and regression lines in the three regions: blue = Main South Indian Ocean (5°N-40°S, 30°E-140°E), green = South Indian Transition (40°S-48°S, 30°E-150°E), and red = Antarctic (Indian Sector) (52°S-70°S, 25°E-165°E). The data from the tangerine areas (48°S-52°S) are excluded from the analysis because of large interannual and spatial variability. The regression equations are listed in Table 1.

analysis because of large spatial and seasonal variability. The subtropical region (green) yields a linear regression line nearly consistent with the E-P line with a small intercept of 28.4 µeq kg^{-1} (Table 1). The waters in the eastern South Pacific (blue) and in the sub-Antarctic zone (magenta) yield large positive intercept values (Table 1) due to the addition of the low-salinity high-PALK waters from the Peru upwelling zone and the Southern Ocean. The mean RMSD for the four regions is ± 7.0 µeq kg^{-1}.

3.2.5. North Indian Ocean: (5° N – 27°N)

The North Indian Ocean is divided into three regions, and the sample locations and data are shown in Fig. 7. All three regions exhibit gentler slopes than the E-P line with positive intercepts (Table 1). The positive

intercept found for the Main North Indian region may be attributed to CaCO$_3$ production in high salinity waters as well as to the input of the fresh Indus River waters with additional PALK. The large positive intercept observed for the Red Sea is due to intense evaporation (high salinity) coupled with CaCO$_3$ production. The Bengal Basin trend is primarily due to the influx of the high PALK Ganges-Brahmaputra River waters. The regression equations are listed in Table 1, and the mean RMSD for these three regions is ± 7.9 µeq kg^{-1}.

3.2.6. South Indian Ocean: (5° N – 70°S)

The South Indian Ocean is divided into four regions (Fig. 8). The PALK-salinity trend (blue plot) for the Main South Indian Ocean region
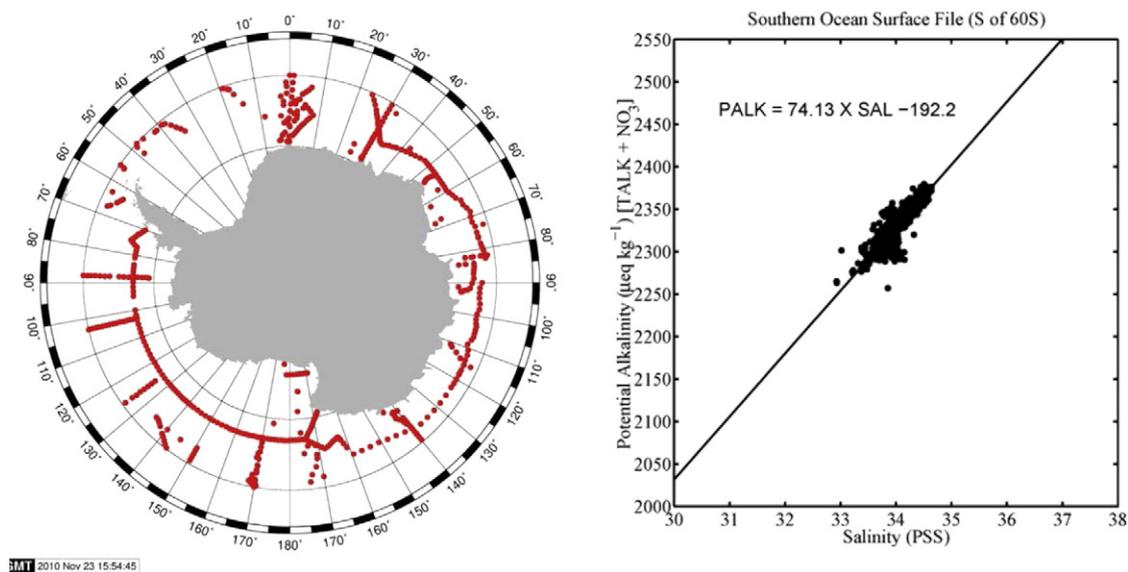
Fig. 9. Sample locations (left) and the PALK-salinity plot (right) for the Southern Ocean south of 60°S. The linear regression line and equation are indicated in the data plot and are used to represent the circumpolar Southern Ocean (see text for explanation).

(5°N-40°S), which covers the subtropical and tropical oceans, has a slope nearly equal to the E-P slope, but with a small positive intercept reflecting the $CaCO_3$ production. The Southern Ocean water has about 100 μeq kg^{-1} greater PALK than the subtropical and tropical waters, due to the upwelling of the deep waters in the Southern Ocean. The flat trend (green plot) for the South Indian Transition zone represents a mixing line between the subtropical and Southern Ocean waters. The mean RMSD for the three regions is ± 6.5 μeq kg^{-1}.

3.2.7. Southern Ocean: (south of 60°S)

The PALK-salinity relationships in each of the Atlantic, Pacific and Indian sectors of the Southern Ocean are analyzed separately in order to examine the differences between the subtropical waters and the polar waters. As shown in Table 1, the regression slopes and intercept values in each of these sectors vary widely: the regression slopes for the Atlantic and Pacific sectors are 57.8 and 81.7 μeq kg^{-1} per salinity unit respectively. This may be attributed to a narrow salinity range (33.0 - 34.6) as well as to uneven seasonal and spatial distribution of samples. However, in the salinity range of 33.0 to 34.6 in Southern Ocean surface waters, these regression equations give PALK values consistent to each other within a mean difference of ± 8 μeq kg^{-1}. Since the differences between the regression lines for the three sectors are not significantly different in this salinity range, the PALK data in the circumpolar surface waters are grouped together (Fig. 9) and represented by a single linear regression line with a RMSD of ± 9.1 μeq kg^{-1} (Table 1): PALK (μeq kg^{-1}) = 74.13 x Salinity (PSS) -192.2. The negative intercept (-192.2 μeq kg^{-1}) may be attributed to greater upwelling of deep waters in higher salinity areas. This relationship is used for the calculation of the distribution of pH and others, rather than the regression lines for each of the Atlantic, Indian and Pacific sectors. Thus, a total of 24 regions are used in this study for the global ocean analysis.

For the salinity correlation, we use PALK ($= TA + NO_3^-$) and neglect the contribution of $HPO_4^=$. In order to test the validity of our analysis, we have computed a regression line using ($TA + NO_3^- + HPO_4^=$) for the same set of the high nutrient waters of the Southern Ocean as used for Fig. 9, and obtained:

$$(TA + NO_3^- + HPO_4^=) = 74.65 \text{ x Salinity -207.9,}$$

where $HPO_4^=$ is taken to be equal to the total phosphate concentration. For a typical NO_3^- and phosphate values of 25.0 μmol kg^{-1} and 2.3 μmol kg^{-1},

the equation above yields TA of 2302.9 μeq kg^{-1} ($= 2330.2 - 25.0 - 2.3$) at a salinity of 34.00. This is consistent with the TA of 2303.1 μeq kg^{-1} ($= 2328.1 - 25.0$) obtained for the same water using the PALK ($= TA + NO_3^-$)-salinity regression in Table 1. The difference of 0.2 μeq kg^{-1} is far smaller than the estimated measurement error of 5 μeq kg^{-1}. Close agreements between TA values from these two methods are observed also for the range of salinity (33.0 – 34.6) in the Southern Ocean. Thus, neglecting $HPO_4^=$ in the PALK-salinity analysis does not bias the results significantly.

3.3. Global Distribution of Total Alkalinity

To obtain pH and degree of saturation for $CaCO_3$, the values for TA and pCO_2 are needed. First, the global distribution of PALK is obtained using its relationship with salinity for the 24 ocean regions (Table 1) and the climatological salinity for the global oceans (Antonov et al., 2010. http://www.nodc.noaa.gov/OC5/WOA09/woa09data.html). Then, the total alkalinity (TA) is obtained by subtracting the climatological mean monthly concentration of NO_3^- (Conkright et al., 1994) from PALK. All the values are reassembled to conform to our 4° x 5° grid for each month. The monthly TA values in 4° x 5° boxes are listed on our web site: GLOBAL pH MAPS & DATA section in www.ldeo.columbia.edu/CO2.

The global distribution of TA thus computed is shown in Fig. 10 for February and August, and the TA values for each of the 12 months are used with pCO_2 data for the computation of other carbonate chemistry parameters. In the gridded data file as well as in Figs. 10, 11, 16, 17, 18 and 19 (for TA, pH, Ωaragonite, Ωcalcite and TCO_2 respectively), the equatorial Pacific boxes, which are marked with "+" in the figures, are left blank. Because of the large and irregular interannual variability induced by the reorganization of ocean dynamics during the El Niño and La Niña events (Feely et al., 2002), the available TA and TCO_2 measurements are not enough to compute reliable mean values for each of these phases separately. In contrast to the equatorial Pacific zone, the dynamics of subpolar-subtropical frontal zones (marked "Transition Zone" without regression lines in Table 1) is dominated by eddy mixing and meandering of the front without major reorganization of ocean dynamics. The large variation of the TA and TCO_2 data are likely to be due primarily to the lateral mixing of the water masses within the transition zone. Accordingly, the mean box values in this zone are approximated by linearly interpolating from the adjacent boxes and marked with dots in the figures.

A) February
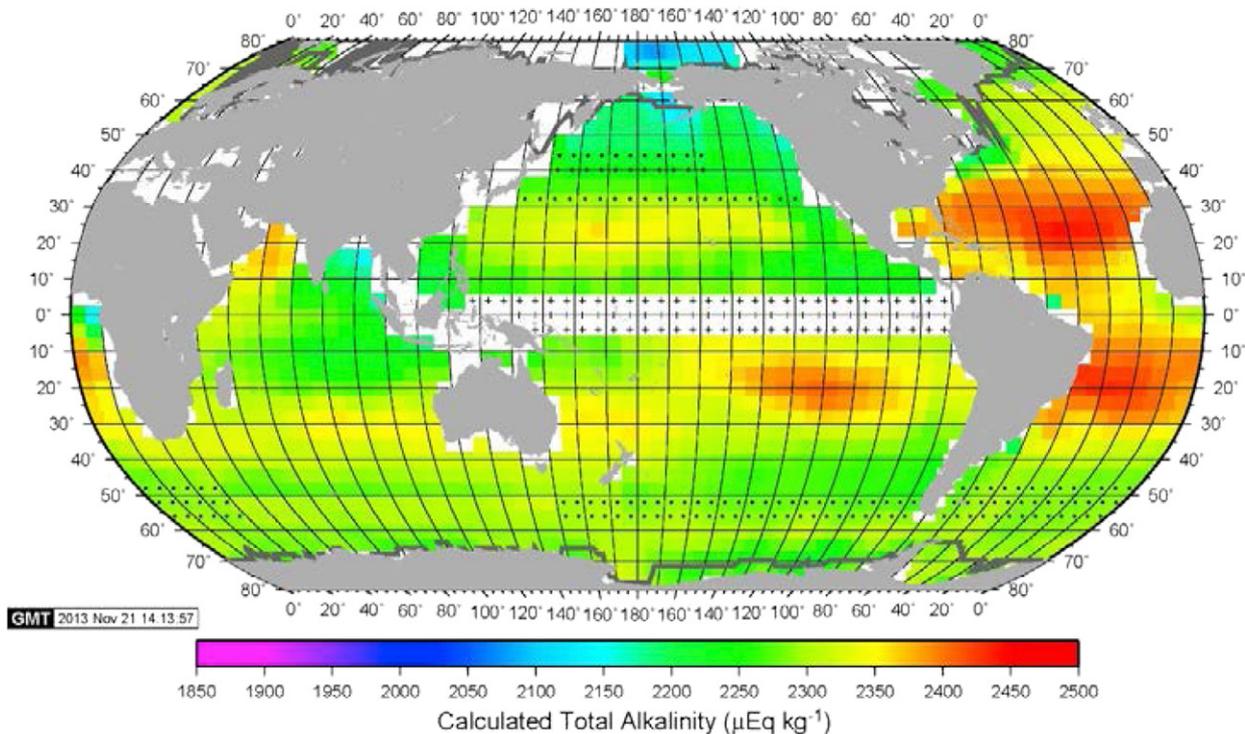
B) August
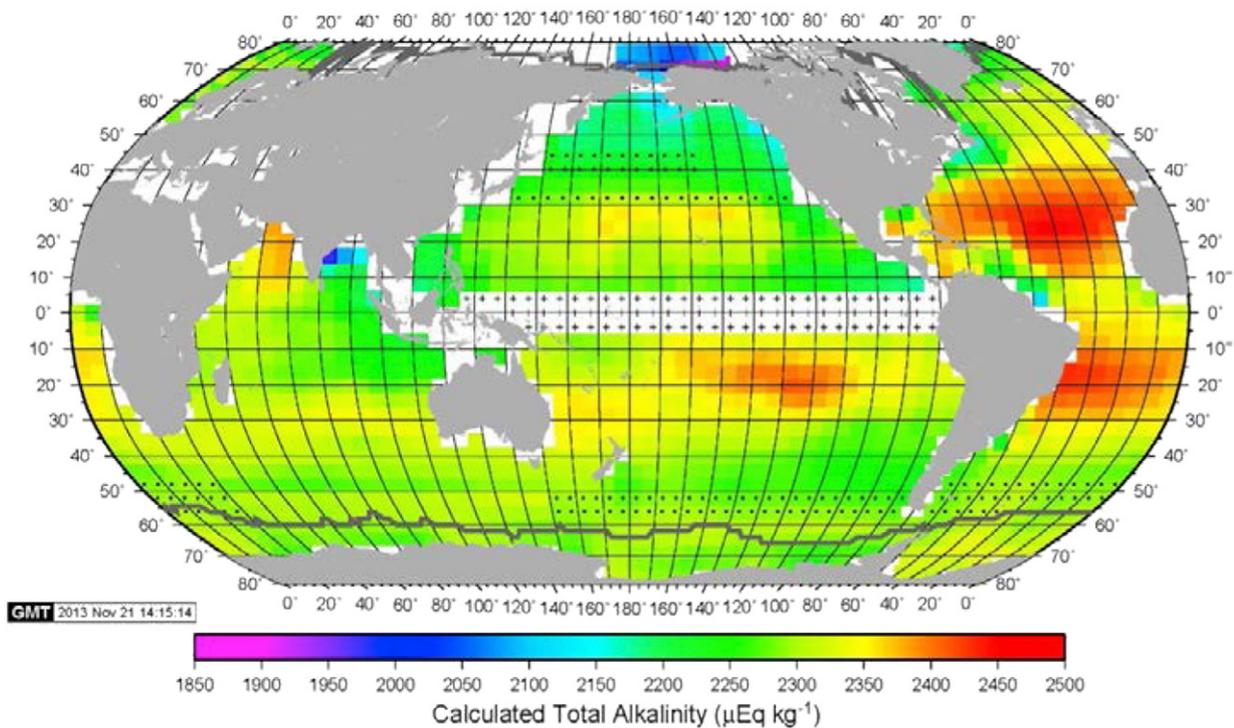
Fig. 10. Climatological mean distribution of the total alkalinity (TA) over the global ocean with a 4° x 5° resolution. The TA values are computed using the potential alkalinity-salinity relationships (measured during 1990-2008) (Table 1) and the climatological mean monthly values for surface water salinity (Antonov et al., 2010) and concentrations of nutrients (Conkright et al., 1994). The black dots indicate transition zones between the subtropical and subpolar waters, where the TA values vary irregularly. The TA values in these areas are interpolated using adjacent pixel values. The equatorial Pacific areas marked with "+" symbols are excluded from the analysis because of the large interannual changes associated with El Niño events. The heavy grey curves in polar regions indicate the mean position of the equator-ward extent of ice field.
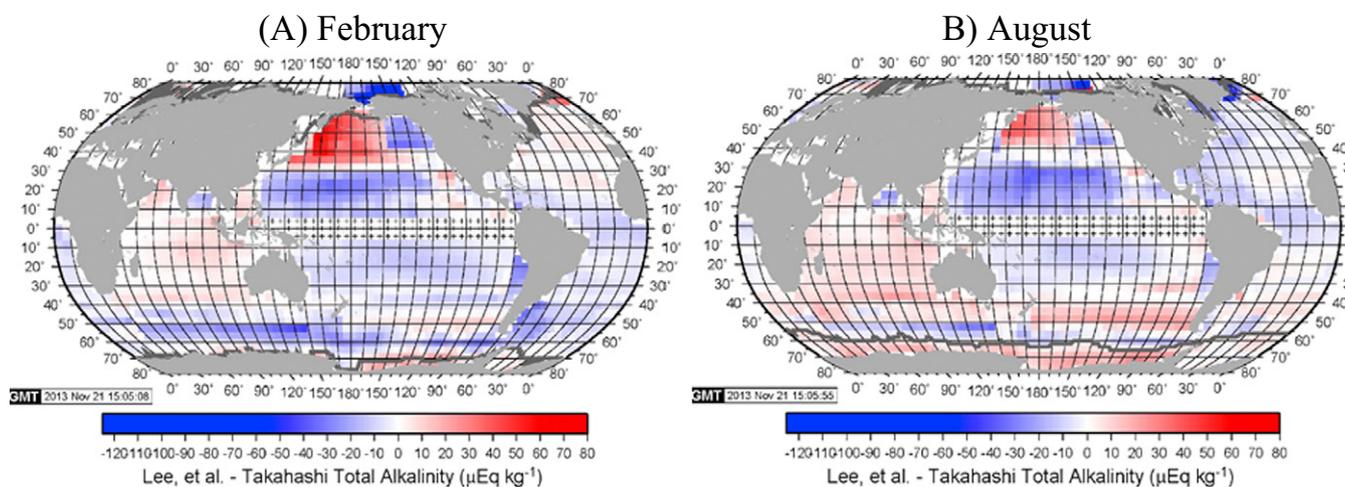
Fig. 11. Differences, (Lee et al. – This study) in μeq kg⁻¹, between the surface water alkalinity values by Lee et al. (2006) and this study: A) February, and B) August. The Lee et al. values are computed using their equations with the climatological mean temperature and salinity data used in this study. No estimates are given for the equatorial Pacific (marked with the "+" symbols). The heavy grey curves in polar regions indicate the mean position of the equator-ward extent of ice field.

Fig. 10 shows that the subtropical North and South Atlantic Oceans have the highest TA values among the global oceans due primarily to the high salinity caused by the high E/P ratios, whereas the tropical and subtropical Indian Ocean has lower values. The high values in the Arabian Sea are due primarily to the upwelling of deep waters, and the low values in the Bay of Bengal (and to a lesser extent, off the mouth of the Amazon and La Plata Rivers) are caused by the low salinity river waters. The low salinity waters (33.5 > Sal > 25.5) for the Bering Sea and the Arctic have the lowest TA values, which are attributable to excess precipitation and ice melting in the region. In contrast to the subarctic and Arctic waters, TA in the Southern Ocean is similar to the mid-latitude waters. This may be due to higher salinity (34.2 > Sal > 33.7) and upwelling of high TA subsurface waters.

The seasonal variation of TA is generally small over the tropical and subtropical oceans, reflecting small changes in salinity and NO_3. Small changes are also found in the subpolar and polar waters, where large seasonal changes as large as 32 μeq kg⁻¹ are anticipated due to seasonal changes in NO_3 and phosphate associated with biological activities. Contrary to the expectation, the observed seasonal changes (Fig. 10) are found to be much smaller, within a range of ± 5 μeq kg⁻¹ in the subpolar regions of the both hemispheres. This may be accounted for by the near cancelation of the salinity effect with the NO_3 effect: TA is decreased by lower salinity in summer (due to decrease in E/P), whereas it is increased by lower NO_3 concentrations in summer (due to biological uptake). For example, in the subarctic western Pacific (54°N-58°N and 162.5°E-157.5°W), TA is reduced by 18 (± 13) μeq kg⁻¹ in summer due to a lowering of summer salinity by 0.3 (± 0.2) PSS, and is increased by 16 (± 2) μeq kg⁻¹ by the reduction of NO_3, resulting in a net reduction of 2 (± 14) μeq kg⁻¹, which agrees with the observed mean reduction of 4 (± 20) μeq kg⁻¹. The salinity effect may exceed the opposing effect of biology or vice versa, and the seasonal amplitude of TA is not only reduced, but also the sign for the seasonal change of TA may be reversed, depending upon the magnitude of changes in salinity and NO_3.

3.3.1. Comparison with Previous Studies

Two major studies on the distribution of TA in the global ocean have been published prior to this study. Analyzing 1,700 surface alkalinity data from GEOSECS, TTO, WOCE and other programs, Millero et al. (1998) divided the world ocean into 6 regions and expressed the salinity-normalized alkalinity as a quadratic function of temperature. More recently, Lee et al. (2006) divided the oceans into 5 regions, and proposed TA formulations for each region as a quadratic function of

both salinity and temperature. In these studies, water temperature was used as a proxy representing the complex oceanographic processes including changes in the net community production, $CaCO_3$ precipitation and dissolution, and lateral and vertical water mixing. In contrast, we divide the oceans into 24 regions, and consider that salinity is the primary driver for alkalinity, and nitrate is a secondary driver reflecting the direct effect on alkalinity of seasonal changes in the net primary production.

Fig. 11 shows a pair of the maps for February and August indicating the differences between the values obtained with Lee et al. (2006) formulations and those from this study expressed as [(Lee et al.) – (This work)]. The Lee et al. values are computed using the same salinity and temperature values as those used in our study. In general, the Lee et al. formulations yield TA values consistent with our estimates on the global average. The tropical and subtropical Atlantic and Indian Oceans are in close agreement. On the other hand, our values for the subtropical Pacific oceans tend to be greater than those of the Lee et al. up to 15 μeq kg⁻¹. In their study, they expressed the subtropical Pacific, Atlantic and Indian Oceans (30°N-30°S) with a single formula, whereas, in our study, each of these three oceans is expressed using a number of region-specific formulas. The differences may be attributed to the Lee et al. method, in which the three oceans are expressed by a single formula.

In the polar and subpolar Southern Oceans, our values differ from Lee et al. seasonally by ± 15 μeq kg⁻¹. In the subarctic and Arctic regions, the Lee et al. values are lower than ours by as much as 50 μeq kg⁻¹. These differences may be attributed to the inclusion of newer data in our study. In the northwestern subarctic Pacific including the Bering Sea (the red areas in Fig. 11), we find that Lee et al. formula yields much greater TA values (up to 60 μeq kg⁻¹) than ours. Lee et al. compared their results with those of Millero et al. (1998), and showed (in Fig. 4 of Lee et al., 2006) that their values in the subarctic Pacific (north of 30°N; their Zone 4) are greater than Millero et al. (north of 30°N; their Zone 5) by as much as 30 μeq kg⁻¹. Our results are more consistent with those of Millero et al. In the Lee et al. formula for the North Pacific (Zone 4), they added "longitude" (the unit unspecified) as an extra parameter for describing the east-west gradient. This parameterization scheme may have caused excessively high TA values in this region.

It should be pointed out that, despite the regional and seasonal differences among these three studies, the respective formulations yield similar RMSD values in a range of ± 5 to ± 9 μeq kg⁻¹, which are consistent with the reported precision of measurements. This suggests that, while these studies used different parameters for fitting the data,

A) February, 2005
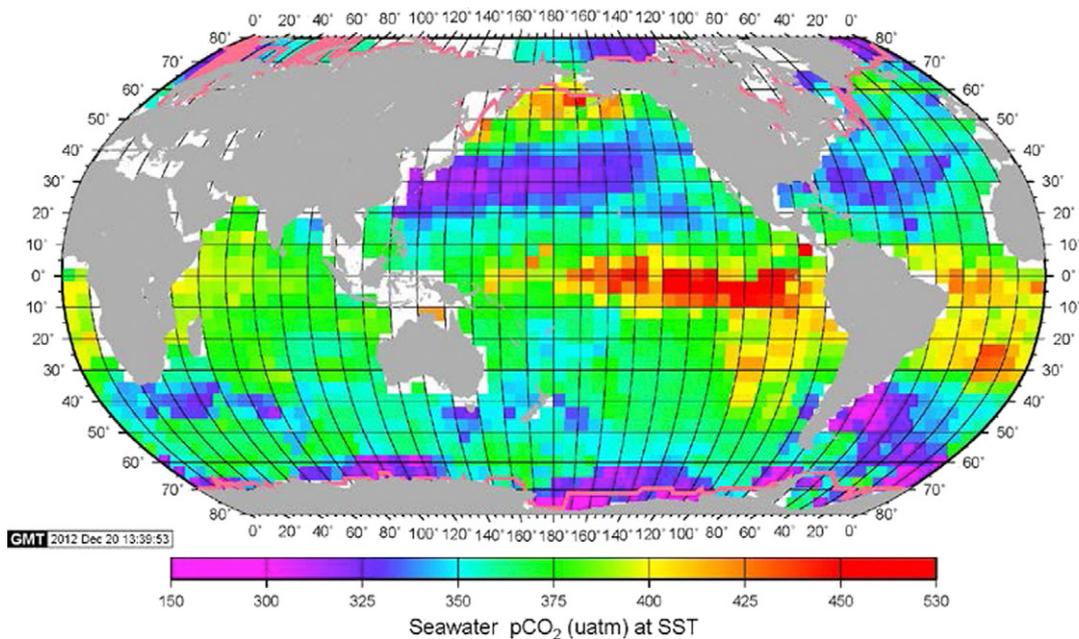
B) August, 2005
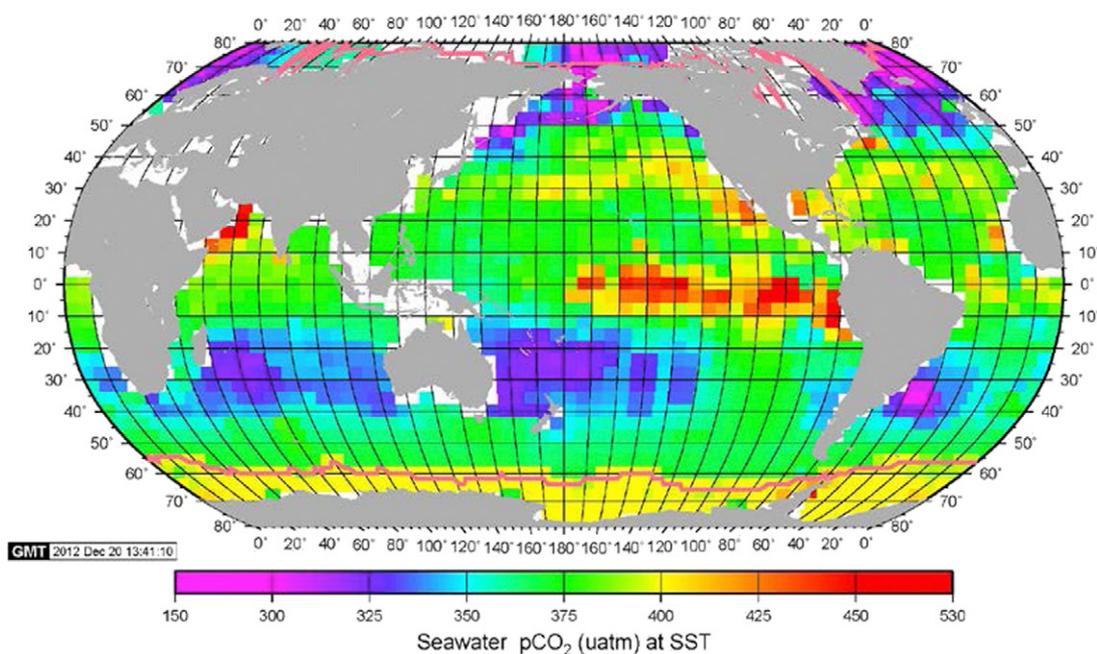
Fig. 12. Climatological mean distribution of the surface water pCO₂ over the global oceans in the reference year 2005: (A) February, and (B) August. These maps have been up-dated to the reference year 2005 using a total of about 5.6 million pCO₂ measurements (Takahashi et al., 2013) which include about 2.5 million new data acquired since 2000. The orange-yellow colors indicate CO₂ source areas for the atmosphere, and the cyan-blue and magenta areas are sink areas for atmospheric CO₂. The heavy pink curves indicate the mean position of the equatorward extent of ice fields.

these methods yield statistically comparable results for the goodness of fit in representing the overall global observations.

3.4. Climatological Distribution of Surface Water pCO₂

For the second carbon chemistry parameter needed for computing pH and related properties, we select pCO₂ in surface ocean water. Its climatological monthly mean values over the global ocean are compiled for a 4° x 5° grid for the reference year 2005, and the gridded data for each of 12 months are available at our web site www.ldeo.columbia. edu/CO2. The February and August values are shown in Fig. 12. This is an updated version of Takahashi et al. (2009) for the reference year 2000 representing non-El Niño years using about 2.5 million new data acquired since then. Of the total of about 6.5 million pCO₂ data observed in 1957-2012 (Takahashi et al., 2013), about 0.2 million for the El Niño periods and 0.6 million for the coastal waters (within 1° x 1° from

(A) 2005 -2000 pCO$_2$ difference (µatm) in February
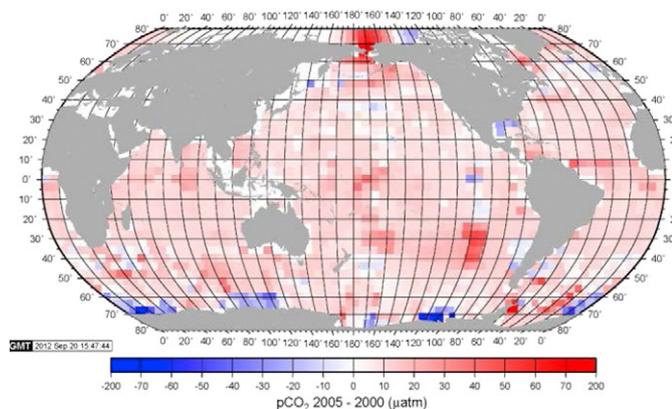
(B) 2005 -2000 pCO$_2$ difference (µatm) in August
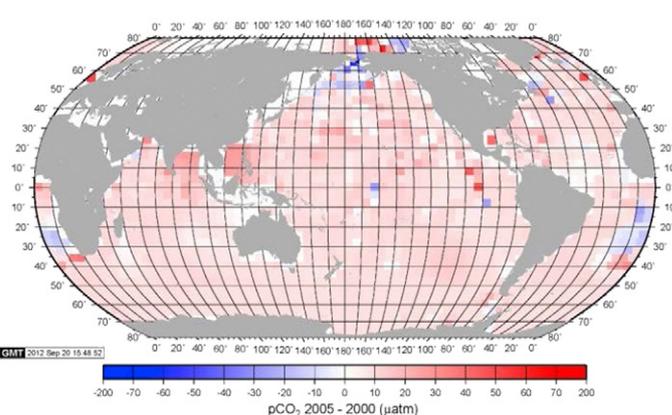
Fig. 13. Differences, (2005 – 2000) in µatm, in surface water pCO$_2$ climatologies between the reference years 2000 and 2005: (A) February and (B) August. Note that the changes are attributable not only to changes occurred in the ocean, but also to the 2.5 million new observations added since the 2000 climatology of Takahashi et al. (2009).
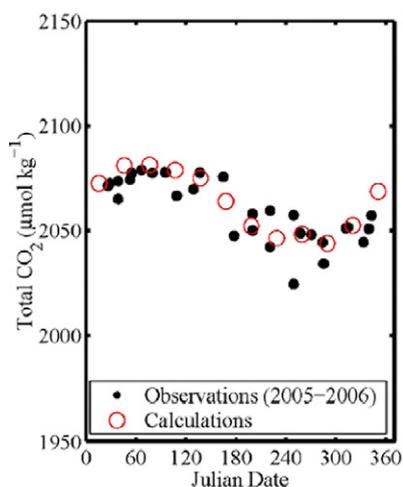
(A) BATS (31.7°N, 64.2°W)   (B) HOT (22.7°N, 158°W)
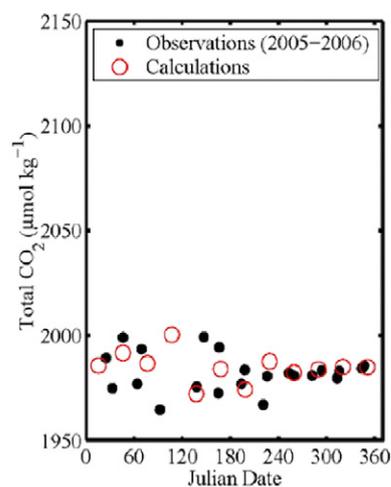
(C) ESTOC (29.1°N, 15.8°W)
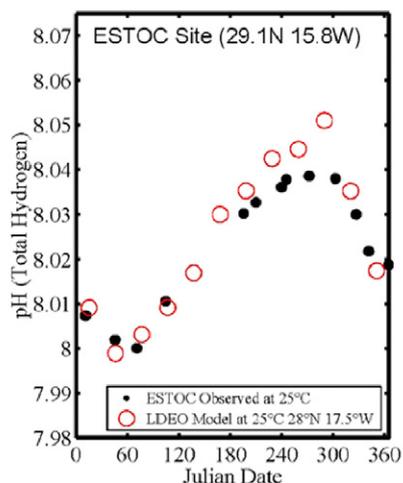
Fig. 14. Comparison of the observed and calculated values at the three time-series stations: A) TCO$_2$ at the BATS station in the western North Atlantic, B) TCO$_2$ at the HOT station in the North Pacific, and C) pH (25 °C) at the ESTOC station in the eastern North Atlantic. The 2005-2006 observations are shown with filled black circles, and the calculated values for 2005 in the 4° x 5° boxes which include these stations are shown with open red circles. The BATS station is located in the 4° x 5° box centered at 32°N and 62.5°W, and the ESTOC station in the box centered at 28°N and 17.5°W. The HOT station is located north of Hawaii near the border of two 4° x 5° boxes, and the computed values for the box centered at 20°N and 157.5°W are shown. The computed TCO$_2$ values are consistent with the observed, capturing the seasonal variability.

land) were removed, and the remaining 5.7 million data are used to compute a climatology for non-El Niño period using the time-space interpolation method (Takahashi et al., 2009) based on a 2-D (x-y) diffusion-advection transport equation.

Large seasonal changes observed in the subtropical gyre areas are attributed primarily to the seasonal temperature changes, whereas the changes in the subpolar and polar areas are due to upwelling of deep waters in winter and intense photosynthesis during summer. The differences between the 2005 and 2000 climatologies are shown in Fig. 13. Compared to the 2000 climatology by Takahashi et al. (2009), the 2005 pCO_2 values are 10 ± 3 μatm greater on the average. The large local differences seen in the polar regions, however, are attributable partially to the improved database, and do not necessarily represent changes which have occurred in the ocean.

4. Validation tests for the estimated values

The validity of our pCO_2-potential alkalinity method is tested by comparing the calculated TCO_2 values with the observed values. We present below a comparison of the monthly values at three well established time-series stations (BATS, HOT and ESTOC) as well as at a number of other areas where some observations are available. Since these time-series data are not included in our "LDEO_SurCarbChem" database, a comparison of the seasonal variation of the measured and computed TCO_2 or pH should provide an independent test for the reliability of the method used in this study.

4.1. Time-series Stations, BATS, HOT and ESTOC

Detailed tests may be made by comparing the monthly observations made during the Bermuda Atlantic Time Series (BATS) program (Bates et al., 2012), the Hawaii Ocean Time-series (HOT) program (Dore et al., 2009; Fujieki et al., 2012), and the European Time Series in the Canary Islands (ESTOC) program (Santana-Casiano et al., 2007; Gonzalez-Davila and Santana-Casiano, 2009). Fig. 14 shows that the computed TCO_2 values for 2005 from the estimated TA and pCO_2 values (open circles) for the BATS and HOT sites reproduce closely the observed values in 2005-2006 (filled circles). For the ESTOC site, the calculated pH values at 25 °C from the pCO_2 and alkalinity are compared with the measured values at 25 °C. Although the computed pH values are higher than the observed by about 0.01 during the later summer months, they are consistent with the observations for the rest of the year. This gives further credence to the pH values obtained by the pCO_2-TA method used in this study.

4.2. Other Ocean Areas

The computed TCO_2 values are compared with the observations in 18 areas located in various ocean regimes. Fig. 15 shows a comparison of the observed TCO_2 data (filled circles) with those computed (open circles) from the 2005 pCO_2 and potential alkalinity-salinity relationships in various oceanographic regimes including the Iceland Sea, Drake Passage, North Atlantic, North Pacific and Indian Oceans. The TCO_2 values were measured in different years. Although TCO_2 has increased at a mean rate of less than 1 μmol kg^{-1} yr^{-1} by the uptake of

A) Subpolar Oceans   B) North Atlantic
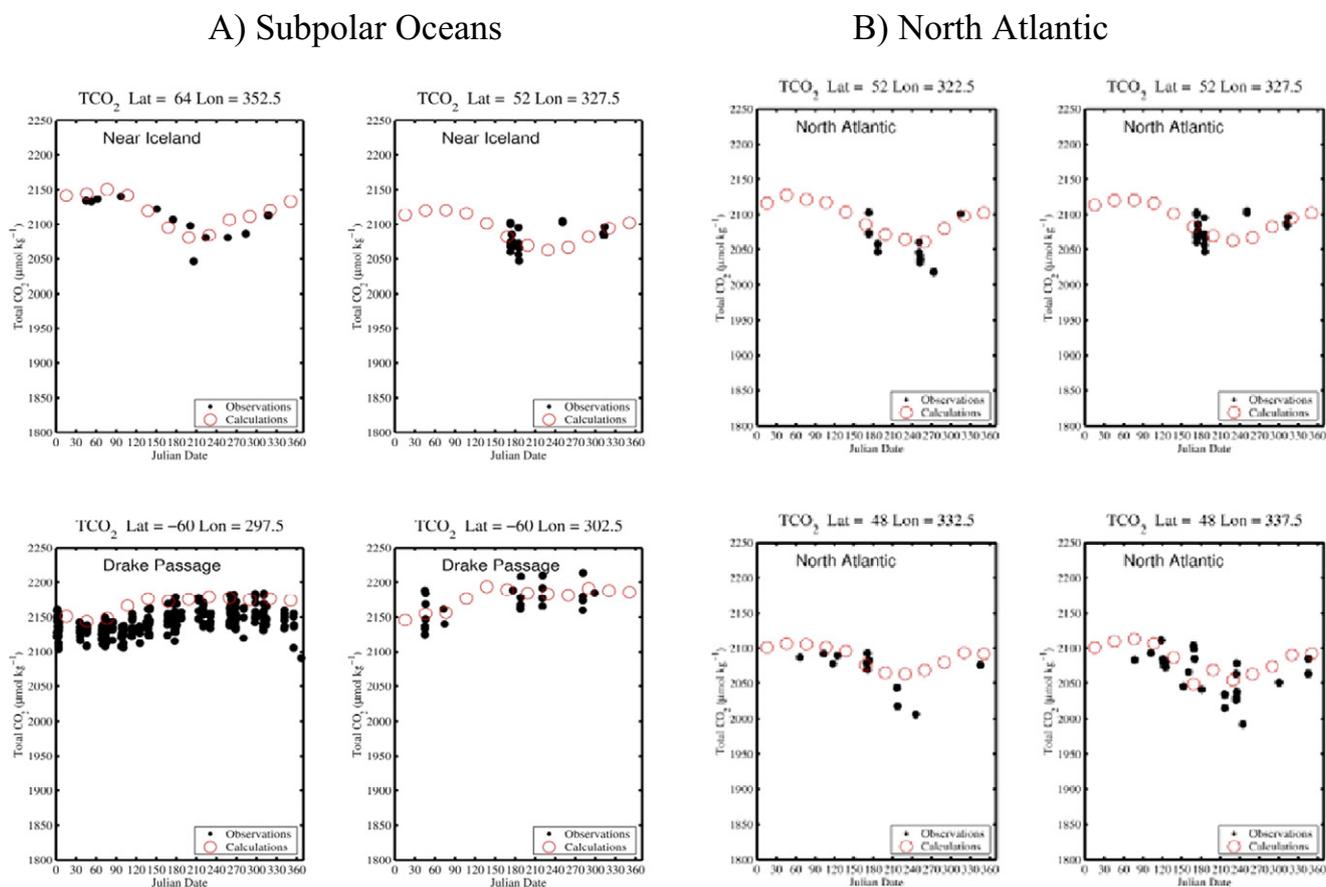
Fig. 15. Comparison of the observed TCO_2 with the climatological mean seasonal variability of TCO_2 in the reference year 2005 in 4° x 5° box areas in (A) the northern (near Iceland) and southern (Drake Passage) subpolar oceans, (B) the North Atlantic, (C) the western subarctic northeast and central Pacific Ocean, (D) the subarctic northwest Pacific and (E) the northern Indian Ocean. The open circles indicate the calculated values for 2005, and the filled circles indicate the observed values without adjustments for changes due to atmospheric CO_2 uptake. The center position of each 4° x 5° box is indicated at the top of each panel. The most of the computed TCO_2 values are consistent with the measured values. The exceptionally large deviations are found in the northwestern Pacific and northern Indian Oceans, where waters of different properties meet and mix.

C) Sub-arctic Northeast and central Pacific
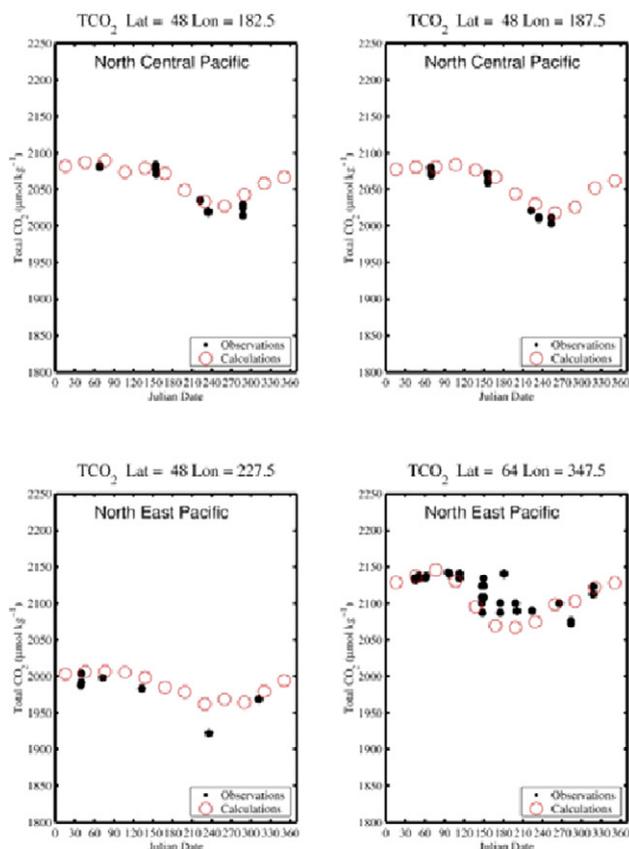
D) Sub-arctic Northwest Pacific
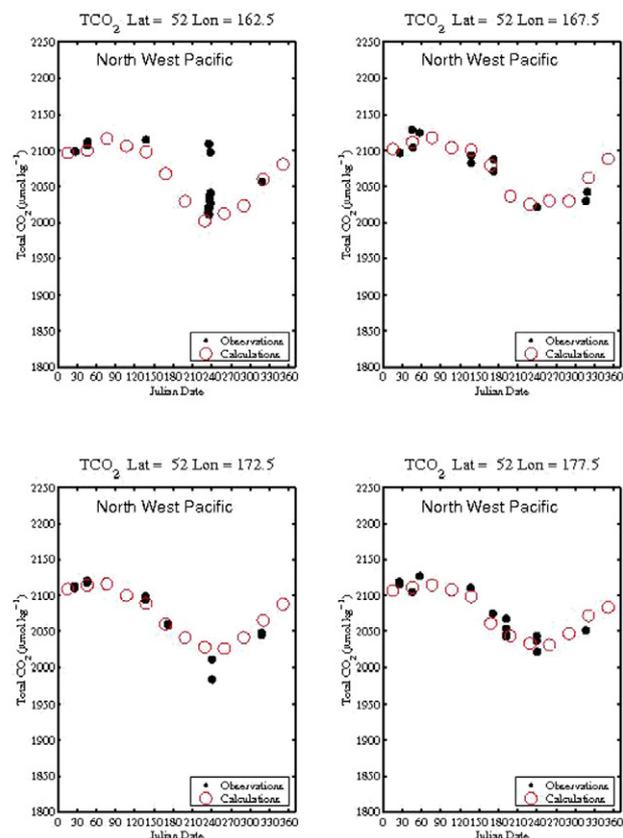
E) North Indian Ocean:
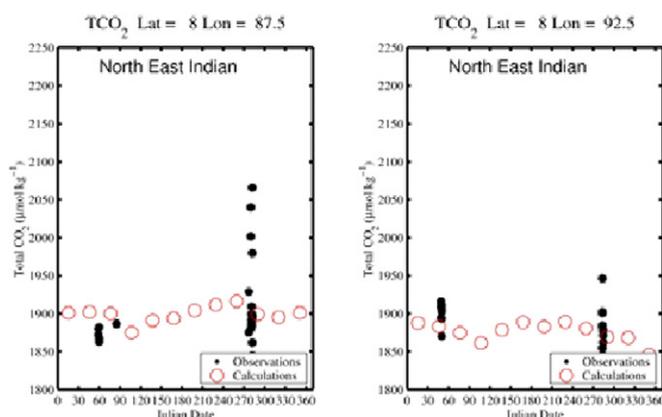
Fig. 15 (*continued*).

atmospheric CO_2, no adjustment is made for the difference between the reference year and year of observation. With the exception of a few ocean areas where different water types meet and mix, the observed TCO_2 values are consistent with those calculated from pCO_2 and PALK. In the northwestern Pacific east of the Kamchatka peninsula (top row, second from right in Fig. 15-D), the observed values near the day 240 (late August) exceed the computed values by as much as 100 μmol kg^{-1}. In this box area, the Oyashio Current is joined by a narrow flow of low-salinity water from the Bering Sea. In the northeastern Indian Ocean (Fig. 15-E), the large deviations seen in the late summer may be attributed to the influx of the Indus River in the Arabian Sea and the Ganges-

Brahmaputra River waters in the Bay of Bengal. These deviations are attributed to erroneous TA values that result from the failure of the PALK-salinity relationships to include the influx of different water types. These small scale structures cannot be adequately represented by the 4° x 5° spatial resolution used in this study, indicating the limitation of this study.

5. Climatological mean distributions

The climatological mean distribution maps for pH, and degree of saturation for aragonite and calcite in surface waters of the global

(A) Calculated pH for February, 2005
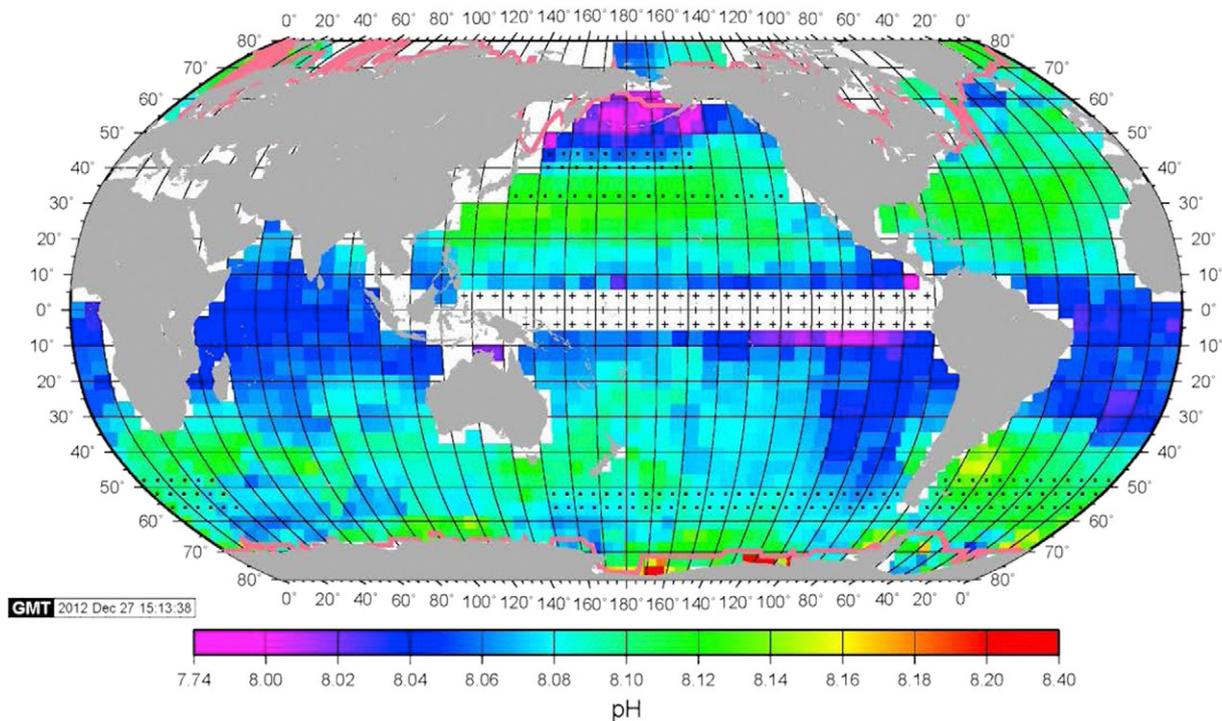
(B) Calculated pH for August, 2005
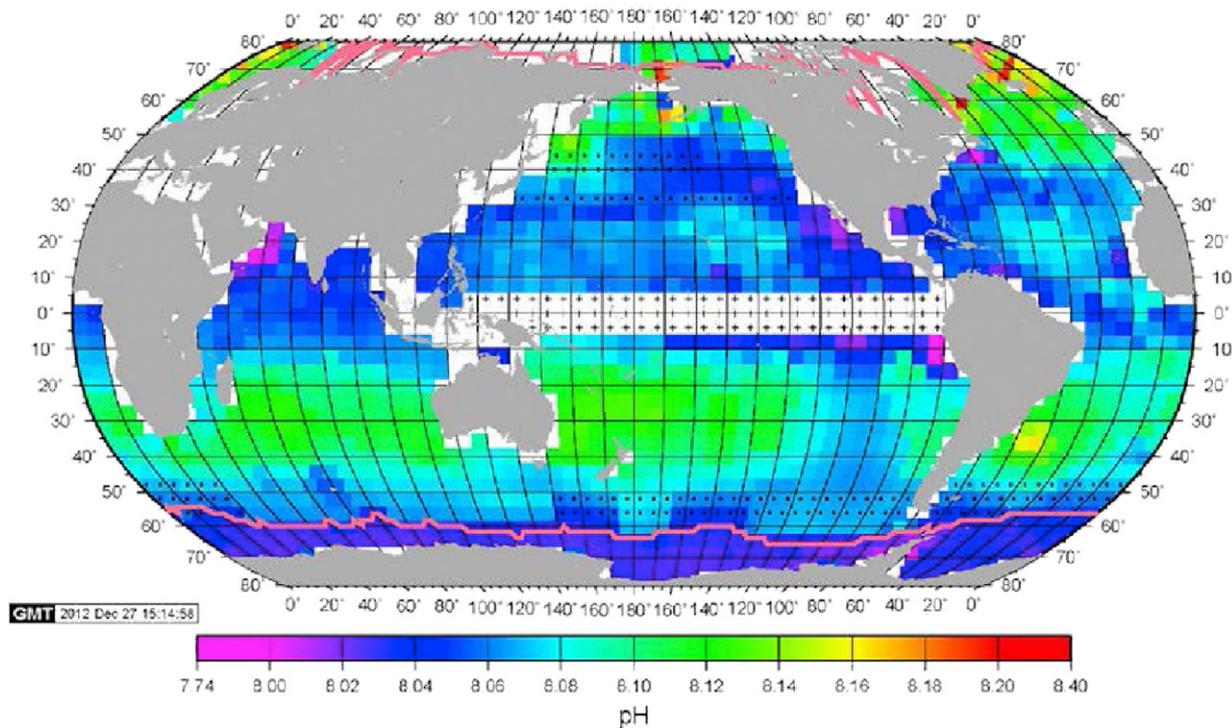
Fig. 16. The climatological mean distribution of pH (total H^+ ion scale at in situ temperatures) in the global ocean surface water in (A) February and (B) August in the reference year 2005. The pink curves indicate the positions of the mean equator-ward front of seasonal ice fields. The "+" symbol indicates the box areas affected by the El Niño events, and no value is given. The boxes with black dots are in transition zone between oceanographic regimes (such as subtropical to subpolar regimes), where the pH values are highly variable. The values in these boxes are interpolated from the adjacent box values.

oceans for the reference year 2005 are presented in this section. These are calculated using the following climatologies; a) climatological mean monthly pCO_2 in surface water in 4° x 5° box areas for the reference year 2005 (see Section 3.4); b) the potential alkalinity-salinity relationships representing 24 oceanic areas (based on the measurements made 1990-2008, Section 3.2); c) climatological mean monthly values for surface water temperature (NCEP Reanalysis data, 2001), salinity (Antonov et al., 2010) and concentrations of nutrients (Conkright

A) February, 2005
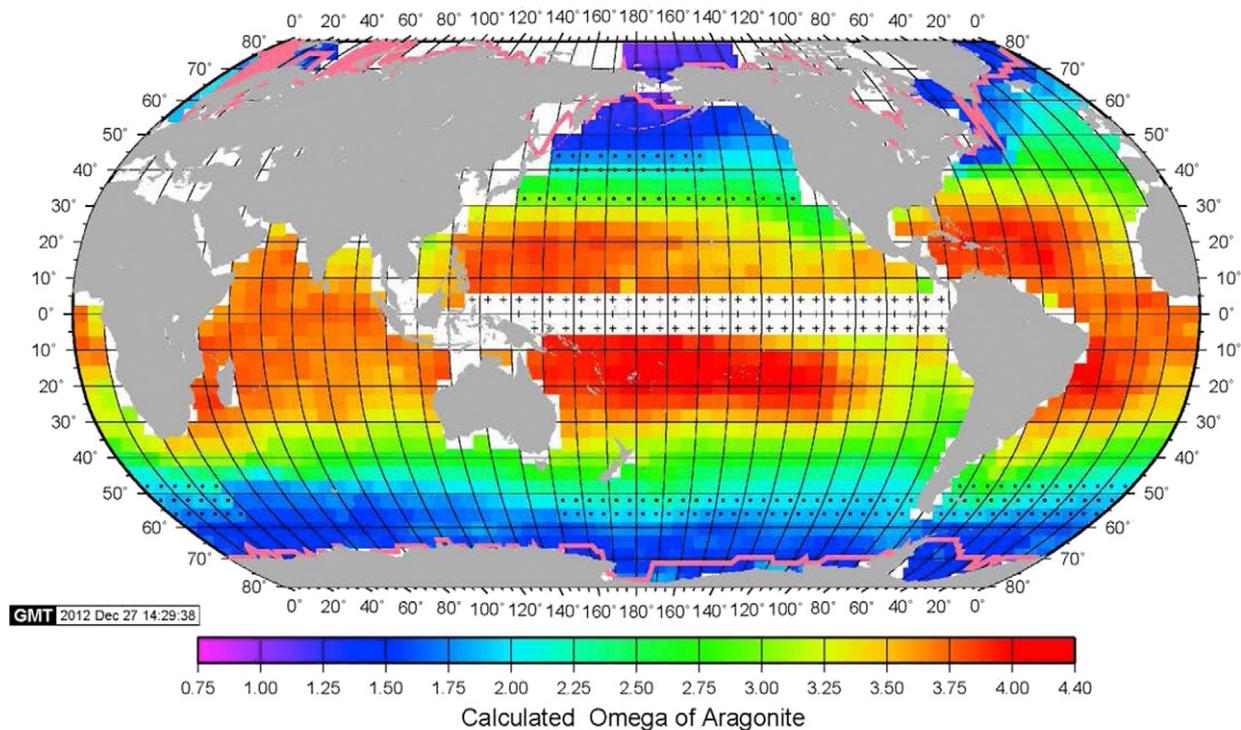
B) August, 2005
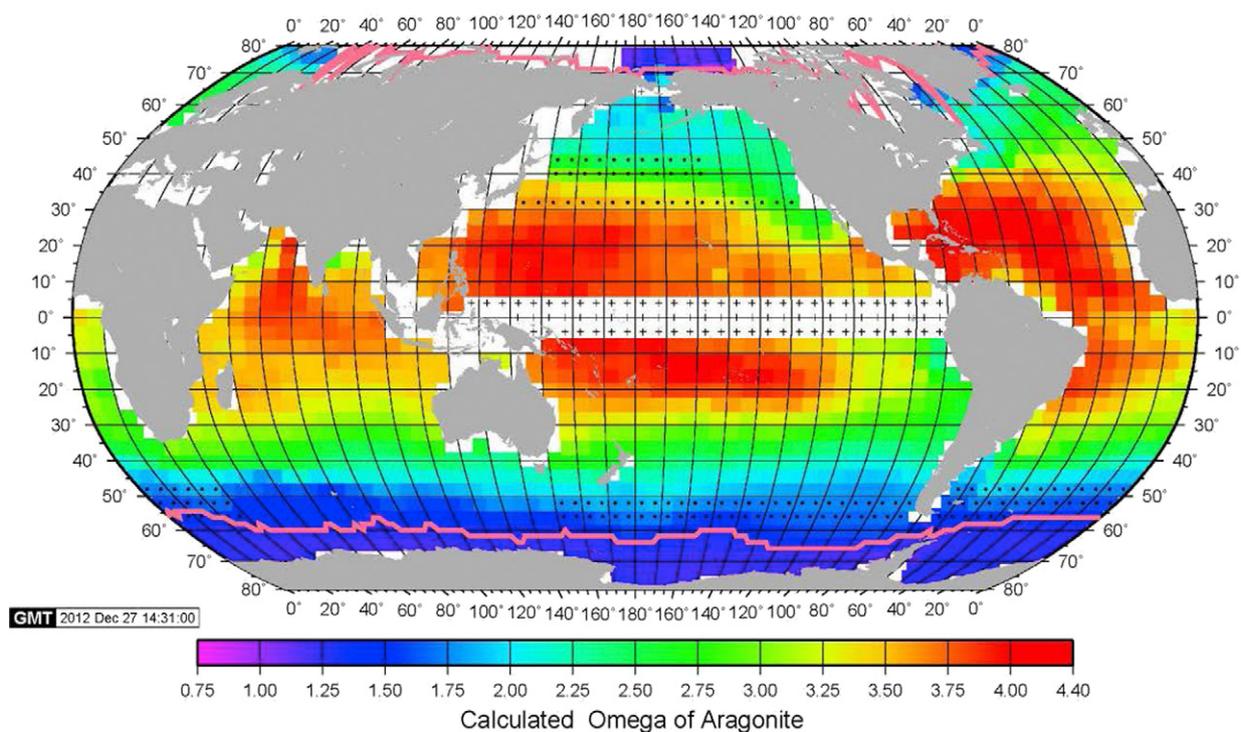
Fig. 17. The climatological mean distribution of aragonite saturation level (Ω) in the global ocean surface water in (A) February and (B) August in the reference year 2005. The pink curves indicate the positions of the mean equator-ward front of seasonal ice fields. The "+" symbol indicates the box areas affected by the El Niño events, and no value is given. The boxes with black dots are in transition zone between oceanographic regimes (such as subtropical to subpolar regimes), where the Ω values are highly variable. These values are interpolated from the adjacent box values. Note that the Arctic Ocean is slightly undersaturated ($\Omega < 1.0$), whereas the seasonal ice zone in the Southern Ocean is 10% to 20% above the saturation.

et al., 1994); and d) the inorganic carbonate chemistry model (Section 2). The degree of saturation for aragonite and calcite is expressed in $\Omega = [Ca^{++}]_{sw} \times [CO_3^=]_{sw} / Ksp'$, where Ksp' is the solubility product for $CaCO_3$ formulated by Mucci (1983) for aragonite and calcite. The calcium concentration in seawater is approximated by $[Ca^{++}]_{sw}$ (mol kg^{-1}) = 0.01012 x (Salinity)/35. $CaCO_3$ supersaturation is indicated by $\Omega > 1.0$, and undersaturation by $\Omega < 1.0$. The 4° x 5° gridded data for each of 12 months are available at our web site, www.ldeo.columbia.edu/CO2 .

On the basis of the estimated uncertainties for TA and pCO₂ of ± 10 μeq kg⁻¹ and ± 10 μatm respectively, the combined uncertainty for each of the computed properties is estimated to be ± 0.01 for pH, ± 0.06 for Ωaragonite, ± 0.09 for Ωcalcite, and ± 10 μmol kg⁻¹ for TCO₂.

5.1. pH

The pH values presented in this paper are in the total H⁺ ion scale, which is the concentration of free H⁺ plus HSO₄⁻ ions (Dickson, 1993), and the distribution at in situ surface water temperature is presented in Fig. 16 for February and August. The values for these and the other months are listed on our web site. The pH values range from 7.9 to 8.2 in 2005. Lower (more acidic) values are found in the upwelling regions in the Panama Basin (in the equatorial Pacific), Arabian and Bering Seas; and higher values are found in the subpolar and polar waters during the spring-summer months of intense photosynthetic production. The vast areas of subtropical oceans have seasonally varying pH values ranging from 8.05 during warmer months to 8.15 during colder months: a 25% change in the H⁺ ion concentration. In contrast, pH in the high-nutrient subpolar and polar waters is lower during winter due to the upwelling of more acidic deep waters, and increases during summer due to intense photosynthetic utilization of CO₂. Accordingly, the seasonal pH change in subpolar oceans is about six months out of phase from that in the adjacent subtropical ocean.

5.2. Degree of Saturation for Aragonite and Calcite

Surface waters of the global oceans are generally supersaturated with respect to aragonite and calcite. As shown in Fig. 17, the warm tropical and subtropical waters are supersaturated with respect to aragonite by a factor of about 4, whereas the cold subpolar and polar waters are supersaturated only by 1.2 (or 20% supersaturation) or less. However, the western Arctic waters become undersaturated in summer with Ωaragonite ranging from 0.9 in summer months to 1.2 in winter months. In recent studies in the western and central Arctic, aragonite undersaturation (Ω as low as 0.8) has been reported (Bates and Mathis, 2009; Bates et al., 2009; Chierici and Fransson, 2009; Robbins et al., 2013). On the other hand, the Southern Ocean waters in the seasonal ice zone are supersaturated with aragonite by 1.3 to 1.5 throughout a year.

Fig. 17 shows that, while the aragonite Ω values for the subtropical Pacific and Atlantic are similar, those in the subtropical Indian Ocean are generally lower (i. e. less saturated, more yellowish in the maps). This reflects the lower pH values (Fig. 16), and the possible causes for the uniqueness of the Indian Ocean will be discussed later in Section 5.4.

The distribution maps of calcite saturation for February and August, 2005, are shown in Fig. 18. The Ω values range between 1.7 in the polar regions to 6.3 in subtropical waters. In the Southern Ocean, the Ω values for calcite are as low as 1.7 in the under-ice waters due to the upward mixing of high CO₂ deep waters, and it is about 2.3 in the seasonal ice zone waters. The global pattern of distribution is similar to that for aragonite, and the north and south Indian Oceans are shown to have lower degree of saturation than the Pacific and Atlantic, as will be discussed in Section 5.4.

5.3. TCO₂ in surface water

The distribution maps of TCO₂ calculated for February and August, 2005, are shown in Fig. 19. The TCO₂ values range between 2,225 μmol kg⁻¹ in polar regions to 1,875 μmol kg⁻¹ in subtropical waters. They are higher during winter reflecting greater upward mixing of high-CO₂ deep waters, and are lower during summer due to biological CO₂ utilization. The amplitude for seasonal change is generally about 75 μmol kg⁻¹ for the subpolar waters, while that for subtropical waters is smaller and correlates with the seasonal SST amplitude. The TCO₂ in under-ice waters in the Southern Ocean is as high as 2,230 μmol kg⁻¹ (Fig. 19-B) because of the upwelling of deep waters and the reduced sea-air CO₂ gas exchange by ice cover.

The north and south Indian Oceans are shown to have lower TCO₂ values than the Pacific and Atlantic. The causes for this feature will be discussed in Section 5.4.

5.4. Regional Variability

Fig. 16 shows that the northern Indian Ocean has lower pH than the subtropical North Pacific and North Atlantic in the corresponding latitudes, especially during the northern winter months. All other carbon chemistry properties north of about 30°S are different from the Pacific and Atlantic Oceans. In the Indian Ocean, TA is lower (Fig. 10) and pCO₂ is higher (Fig. 12) than the Atlantic and Pacific. The computed properties including pH (Fig. 16), Ω for aragonite and calcite (Figs. 17 and 18) and TCO₂ (Fig. 19) are all lower in the Indian Ocean than the Atlantic and Pacific reflecting these differences. The causes for these differences are not understood because of the complexity which is unique to the Indian Ocean. In the northwestern Indian Ocean, the Arabian Sea receives a number of different waters including a) the intense summer upwelling of deep waters, b) high salinity warm outflow waters from the Red Sea and Persian Gulf, and c) the Indus River waters. The northeastern Indian Ocean and the Bay of Bengal receive the low salinity Indonesian outflow from the east and the Ganges-Brahmaputra River waters from the north. The proportions of these waters vary seasonally as well as annually. The Arabian Sea water is generally warmer and saltier than the Bay of Bengal. Furthermore, the surface water circulation is reorganized extensively in response to the monsoons. Biological differences, which reflect these physical and chemical differences, may play a role in regulating the carbon chemistry in Indian Ocean waters. Further observational and model studies are needed for improved understanding of the uniqueness of the Indian Ocean.

Significant differences between the subarctic Pacific and Atlantic are shown for the alkalinity (Fig. 10), pH (Fig. 16), the CaCO₃ saturation (Figs. 17 and 18) and TCO₂ (Fig. 19). The role of the large scale ocean circulation on biogeochemical contrasts between the Pacific and Atlantic has been presented extensively in ocean circulation model studies (e. g. Gruber et al., 2009). In the Atlantic, the warm saline Atlantic surface water with high alkalinity flows northward into the GIN Seas and the Arctic basin. In the Pacific, the northward transport of the less saline open Pacific water into the Bering Sea is partially impeded by the Aleutian Arc, and the flow of the Bering Sea water into the Arctic basin is restricted ranging between 0.7 Sv and 1 Sv (Woodgate et al., 2006), due to the shallow Bering Strait. Very large seasonal changes observed in the Bering Sea may be attributed to the long residence time of waters over the broad shallow shelf areas, where pH and CaCO₃ saturation level are lowered by vertical mixing of subsurface waters during winter and are increased by intense photosynthesis in summer (Walsh et al., 1989; Cross et al., 2012; Cross et al., 2013).

6. Time trend

Based upon the multi-decadal time-series observations of carbon chemistry, the mean decadal rate of changes for pH, pCO₂ and degree of CaCO₃ saturation in surface waters has been estimated by Bates

A) February, 2005
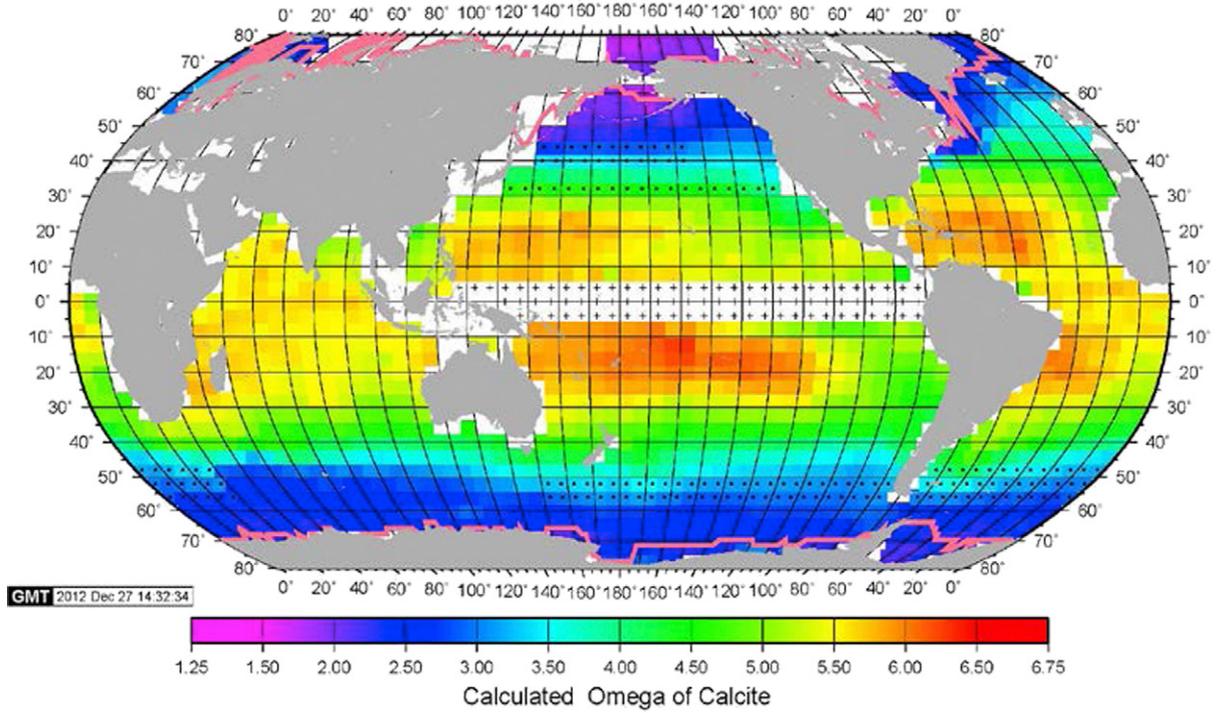
B) August, 2005
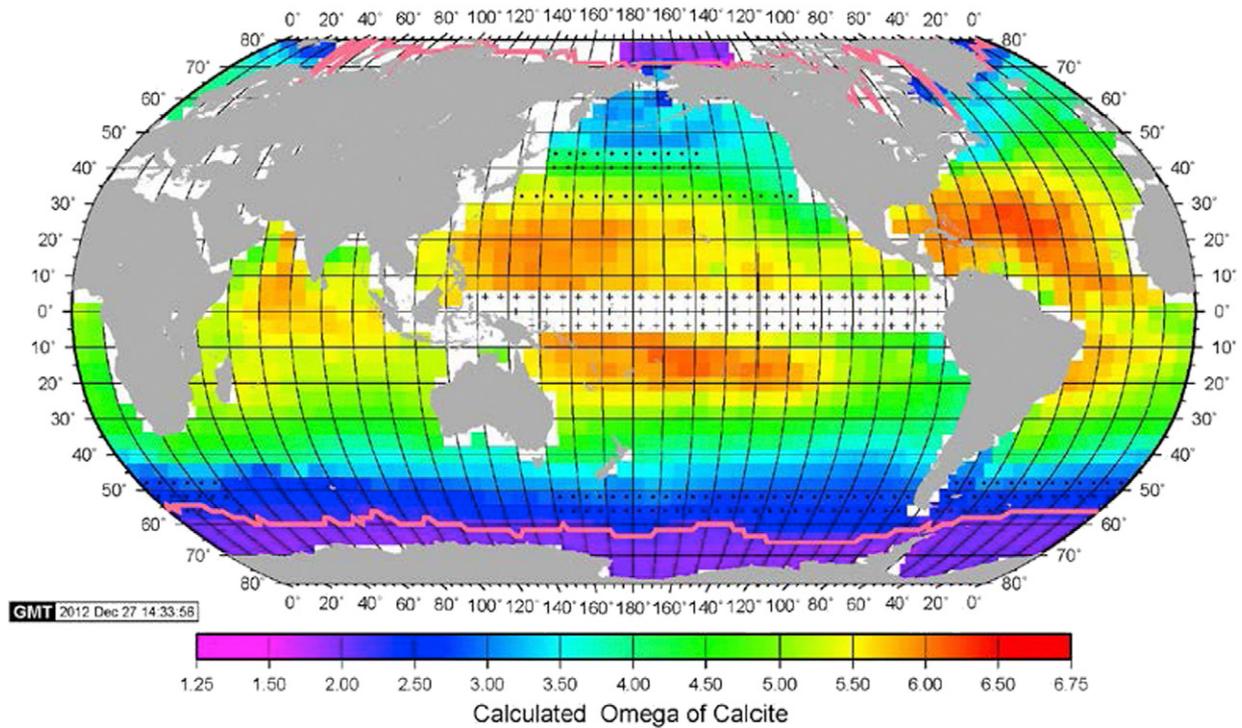
Fig. 18. The climatological mean distribution of calcite saturation level (Ω) in the global ocean surface water in (A) February and (B) August in the reference year 2005. The pink curves indicate the positions of the mean equator-ward front of seasonal ice fields. The "+" symbol indicates the box areas affected by the El Niño events, and no value is given. The boxes with black dots are in a transition zone between oceanographic regimes, where Ω values are highly variable. These values are interpolated using the adjacent box values.

et al. (2012) at BATS in the western North Atlantic; Santana-Casiano et al. (2007) at ESTOC in the eastern North Atlantic; Dore et al. (2009) at HOT in the central North Pacific; Midorikawa et al. (2010) in the western North Pacific; Olafsson et al. (2009) in the Iceland Sea; and Midorikawa et al. (2012) in the Southern Ocean south of Australia (Table 2). In addition, the 2002-2012 decadal time-series data obtained

A) February, 2005
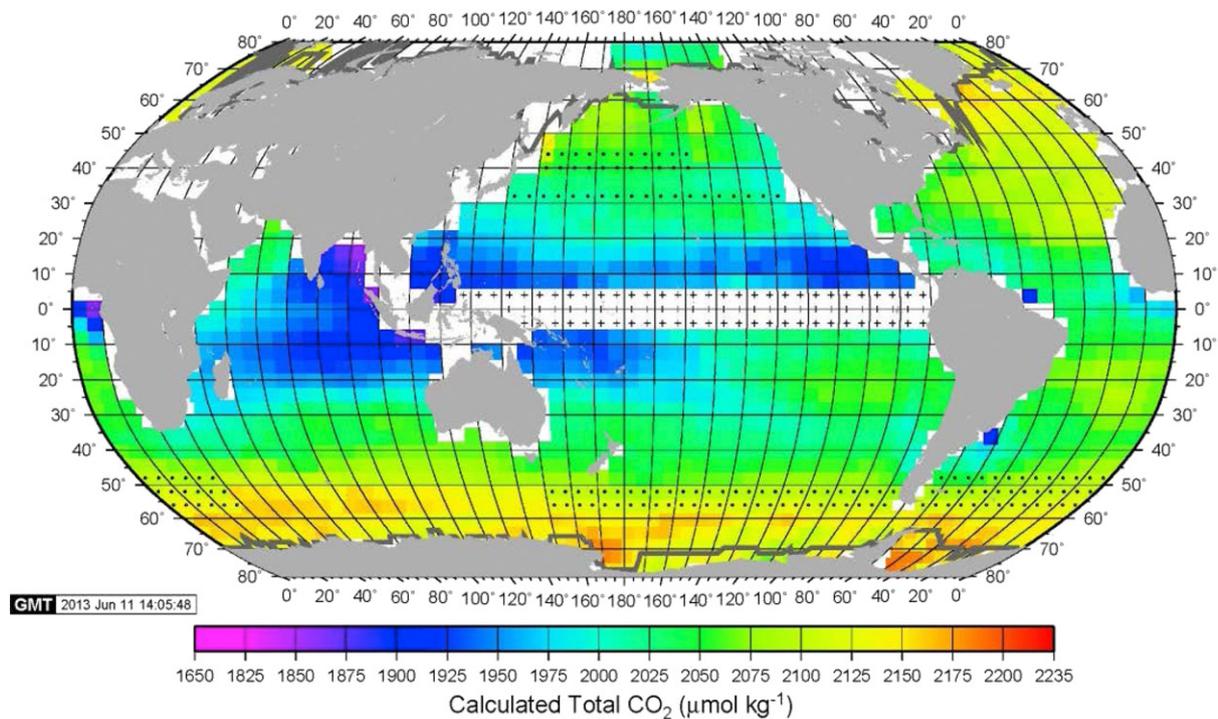
B) August, 2005
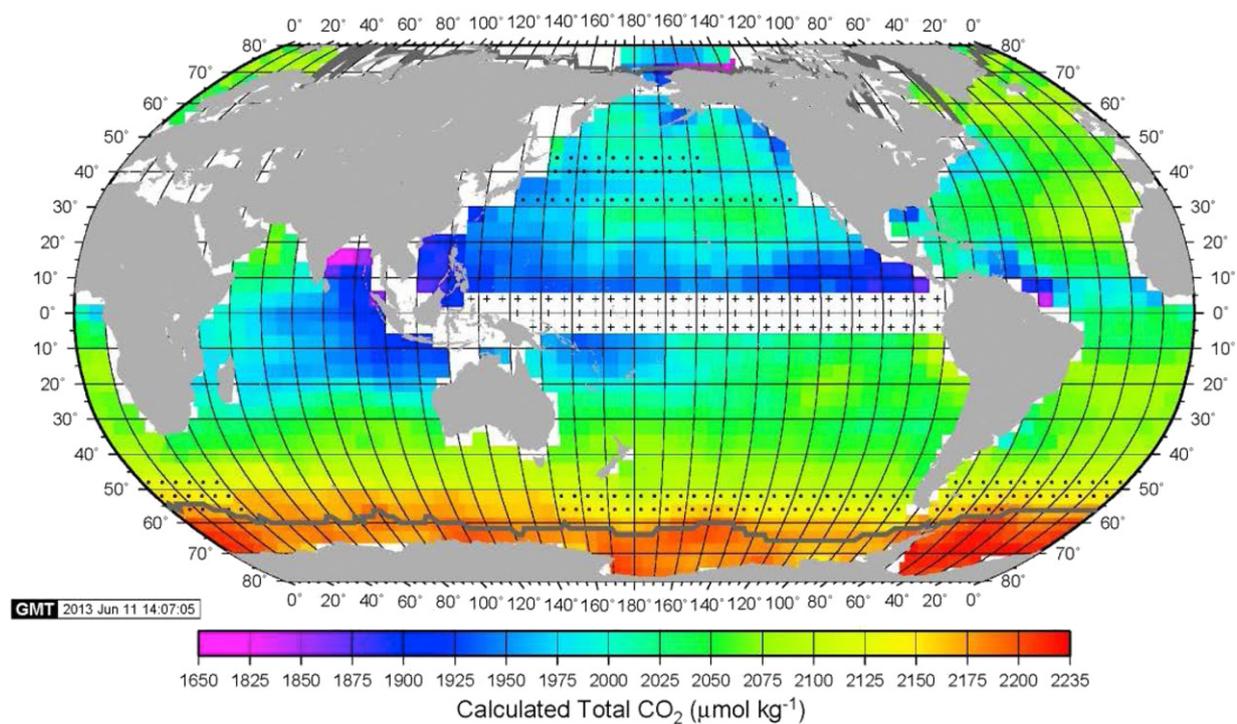
Fig. 19. The climatological mean distribution of TCO$_2$ in the global ocean surface water in (A) February and (B) August in the reference year 2005. The TCO$_2$ values are computed using the total alkalinity (TA) and pCO$_2$. The grey curves indicate the positions of the mean equator-ward front of seasonal ice fields. The "+" symbol indicates the box areas affected by the El Niño events, and no value is given because of large space-time variability. The boxes with black dots are in transition zone between oceanographic regimes (such as subtropical to subpolar regimes), where TCO$_2$ values are highly variable. These values are interpolated using the adjacent box values.

Table 2

Mean decadal rate of change in eight properties at selected time-series observations. The locations are arranged in a general order of north to south. The values in *italics* are the values reported in Olafsson et al. (2009), Bates et al. (2012), Santana-Casiano et al. (2007), Dore et al. (2007), Midorikawa et al. (2010) and Midorikawa et al. (2012) respectively. "NR" means "Not Reported" in the original papers. The **bold-faced** entries are the values that are computed using the updated observations provided by the investigators at the respective stations. The rates are given in per decade.

Location	SST	Salinity	TA	TCO$_2$	pCO$_2$	pH (total H$^+$)	Ωaragonite	Ωcalcite
	°C decade^{-1}	PSS decade^{-1}	(μeq/kg) decade^{-1}	(μmol/kg) decade^{-1}	μatm decade^{-1}	decade^{-1}	decade^{-1}	decade^{-1}
Iceland a/	NR	NR	NR	*14.4 ± 2.3*	*21.5 ± 1.6*	*-0.024 ± 0.002*	*-0.07 ± 0.01*	*-0.12 ± 0.01*
BATS b/	**-0.047 ± 0.21**	**0.055 ± 0.01**	**4.7 ± 0.7**	**15.5 ± 1.2**	**17.8 ± 2.2**	**-0.018 ± 0.002**	**-0.11 ± 0.01**	**-0.16 ± 0.02**
c/	*-0.075 ± 0.21*	*0.058 ± 0.01*	*4.8 ± 0.7*	*13.9 ± 0.6*	*18.0 ± 0.9*	*-0.016 ± 0.002*	*-0.10 ± 0.01*	*-0.15 ± 0.02*
ESTOC d/	**0.23 ± 0.39**	**-0.01 ± 0.02**	**-0.95 ± 1.2**	**9.5 ± 1.4**	**20.8 ± 3.8**	**-0.020 ± 0.004**	**-0.10 ± 0.02**	**-0.15 ± 0.03**
e/	*0.02 ± 0.19*	*-0.09 ± 0.03*	*-7.9 ± 1.4*	*9.9 ± 2.0*	*15.5 ± 4.3*	*-0.017 ± 0.004*	NR	NR
HOT f/	**0.13 ± 0.12**	**0.13 ± 0.02**	**9.5 ± 1.3**	**17.5 ± 1.3**	**18.9 ± 1.3**	**-0.018 ± 0.001**	**-0.08 ± 0.01**	**-0.12 ± 0.01**
g/	*0.26 ± 0.16*	NR	*-0.6 ± 0.6*	*8.5 ± 0.8*	*18.8 ± 1.6*	*-0.019 ± 0.002*	NR	NR
N. Pacific h/	*0.05 ± 0.28*	NR	NR	*9.3 ± 3.0*	*14.8 ± 3.5*	*-0.015 ± 0.005*	NR	NR
Drake Area1 i/	**-0.2 ± 0.5**	**0.02 ± 0.04**	**-0.5 ± 2.3**	**9.9 ± 5.6**	**22.1 ± 5.5**	**-0.023 ± 0.007**	**-0.09 ± 0.05**	**-0.15 ± 0.08**
S.O. SAZ j/	*0.1 ± 0.2*	*0.05 ± 0.06*	*-1 ± 3*	*5 ± 3*	*10 ± 2*	*-0.010 ± 0.004*	NR	NR
Drake Area 4 i/	**-0.6 ± 0.6**	**0.07 ± 0.05**	**6.0 ± 3.1**	**13.1 ± 6.7**	**15.0 ± 6.5**	**-0.015 ± 0.008**	**-0.06 ± 0.05**	**-0.09 ± 0.08**
S. O. PZ j/	*0.1 ± 0.2*	*-0.02 ± 0.04*	*-1 ± 3*	*6 ± 4*	*12 ± 2*	*-0.013 ± 0.003*	NR	NR

a/ Mean for 1985-2008, Iceland Sea Time Series at 68.0°N and 12.67°W, Olafsson et al. (2009).
b/ Mean for 1983-2010 based on the recomputed data for BATS.
c/ Mean for 1983-2011, at BATS, Bates et al. (2012).
d/ Mean for 1996-2010 based on the recomputed data for ESTOC.
e/ Mean for 1996-2004, at ESTOC, Santana-Casiano et al. (2007).
f/ Mean for 1988-2009 based on the recomputed data for HOT.
g/ Mean for 1988-2007, at HOT, Dore et al. (2009).
h/ Mean for 1994-2008, western N. Pacific, 3°N-33°N along 137°E, the summer and winter trends combined, Midorikawa et al. (2010).
i/ Mean for 2002-2012, all seasons (March 2002 through March 2012). Drake Area 1 is an area across the Drake Passage (Fig. 21-B) south of the Sub-Antarctic Front (SAF) and north of the Antarctic Polar Zone (APF); and Drake Area 4 is an area south of the APF. The data are from the LDEO CO2 data archive.
j/ Mean for 1969-2003, the Pacific sector of Southern Ocean (S.O.) 140°E-160°E, austral summer data only, Midorikawa et al. (2012). SAZ = Sub-Antarctic Zone (45°-53°S), PZ = Polar Zone (55°-62°S).

by the LDEO-University of Colorado group across the Drake Passage, Southern Ocean, are shown and discussed in this section. At the BATS and HOT sites, TA and TCO$_2$ were measured, and the pCO$_2$, pH and Ω values are computed. At the ESTOC site, TA and pH (at 25 °C) were measured, and the TCO$_2$, pCO$_2$, pH (at in situ temperature) and Ω values are computed. At the Drake Passage sites, TCO$_2$ and pCO$_2$ were measured, and TA, pH and Ω values are computed. Consistent with the data used in this study, the TCO$_2$ measurements made at these sites as well as those made by Midorikawa et al. (2010), Midorikawa et al. (2012) and Olafsson et al. (2009) are all based on the Certified Reference Solutions of Dickson (2001); the pCO$_2$ measurements are calibrated using the WMO CO$_2$-air gas standards.

6.1. Mean Rate of Change

6.1.1. Atlantic and Pacific Oceans

The updated observations provided by the respective investigators at the BATS, ESTOC and HOT sites are presented in Fig. 20. The calculated quantities are obtained by re-computing the data using the carbonate chemistry model described in Section 2. The decadal mean rates of change for SST, salinity, TA, TCO$_2$, pCO$_2$, pH and Ω are estimated using a linear regression for the updated values and are listed in Table 2. Although the mean rates vary with duration of the time-series data used (Fay and McKinley, 2013), we choose to compute a mean rate for the entire time period of the available observations at each site. The original estimates by Bates et al. (2012) for BATS, by Santana-Casiano et al. (2007) for ESTOC, and by Dore et al. (2009) for HOT are listed with *italics* in the table. Our re-computed rates are mostly in agreement with the earlier studies within the respective uncertainties. The disagreements found for the TA and TCO$_2$ values at HOT may be attributed to the 1997-2000 shift in natural variations related to the Pacific Decadal Oscillation; those found for TA and TCO$_2$ at ESTOC may be due to the shorter 1996-

2004 data used by Santana-Casiano et al. (2007) than the 1996-2010 data (provided by M. Gonzalez-Davila) used for this study.

The BATS and ESTOC sites are located in the subtropical gyres in the North Atlantic, and HOT in the North Pacific. While TA and TCO$_2$ are changing at different rates at these sites reflecting the regional differences in the oceanographic environment, the mean rates of changes for pH, pCO$_2$ and Ω at these sites are statistically indistinguishable: -0.018 to -0.020 decade^{-1} for pH, 18 to 21 μatm decade^{-1} for pCO$_2$, and -0.08 to -0.10 decade^{-1} for Ωaragonite. Furthermore, the rates of change estimated for the Iceland Sea station (68.0°N and 12.67°W) in the subarctic waters (-0.024 ± 0.002 pH decade^{-1} and 21.5 ± 1.6 μatm decade^{-1}; Olafsson et al., 2009) are similar to those obtained at the three major subtropical time-series stations as summarized in Table 2. This may be the result of the surface waters in the southern Iceland Sea being mainly derived from the northward flow of the North Atlantic waters. The rates observed by Midorikawa et al. (2010) for the tropical/subtropical waters in the western-most North Pacific along 137°E between 3°N and 33°N (-0.015 ± 0.005 pH decade^{-1} and 14.8 ± 3.5 μatm decade^{-1}) are also similar to the other subtropical gyre values (Table 2).

6.1.2. Drake Passage, Southern Ocean

Fig. 21-A shows the 2002-2012 time-series data within two selected areas in the Drake Passage, which are roughly parallel to the Antarctic Polar Front (Moore et al., 1999) and the Antarctic Circumpolar Current (ACC). Fig. 21-B shows the data locations: Area 1 (mean SST, 4.8 ± 0.9 °C) is selected to represent the ACC, and Area 4 (mean SST, 0.1 ± 1.4 °C) is chosen to represent the cold Antarctic Polar Water south of the Polar Front. TA is computed using the measured values of pCO$_2$, TCO$_2$, phosphate, silicate, salinity and temperature. When the phosphate and silicate values are missing, mean monthly values in each area are used. The errors in TA due to this substitution are 1 μeq kg^{-1} or less. Since the data from Areas 2 and 3 vary irregularly due to eddy mixing
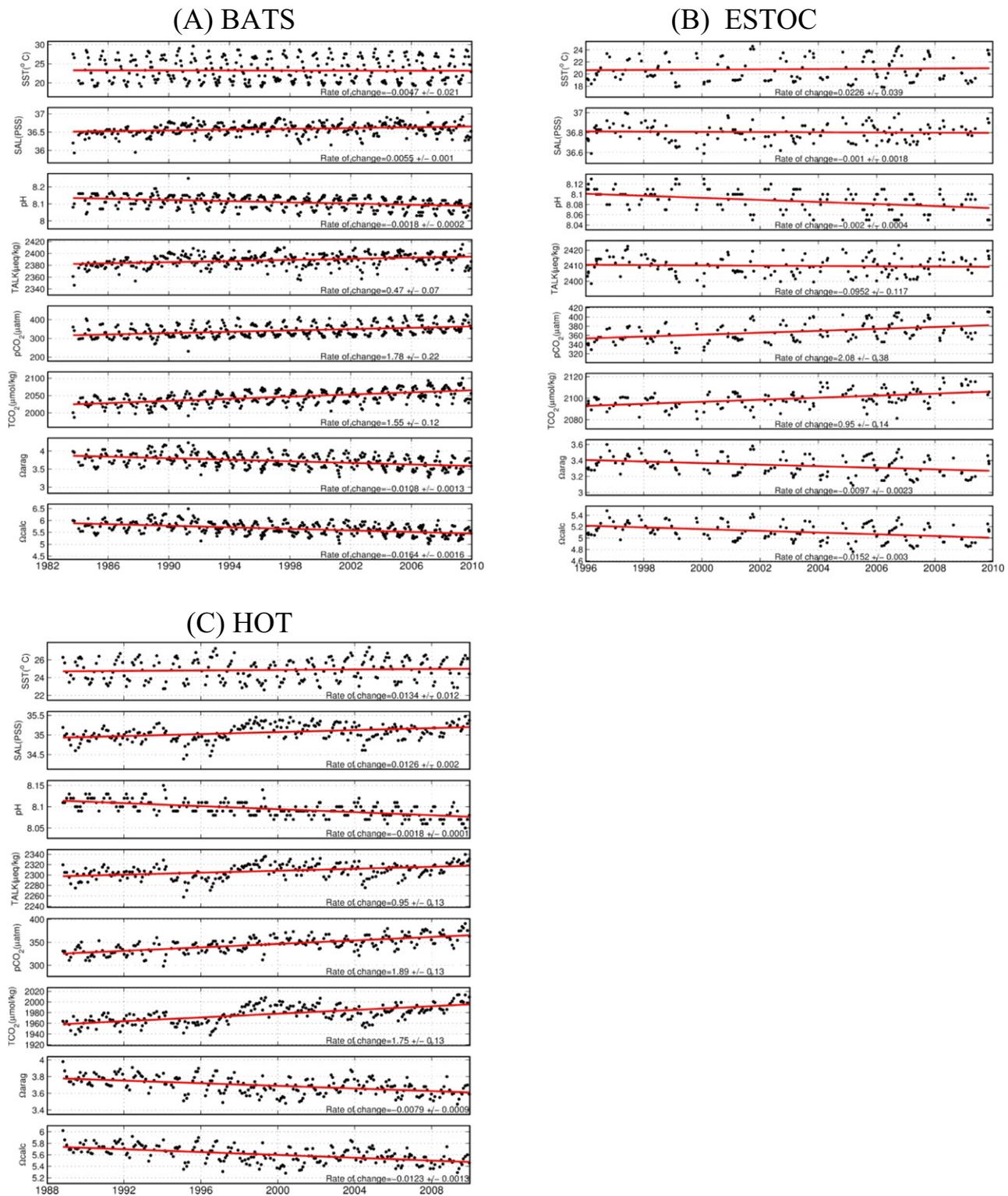
(A) BATS

(B) ESTOC

(C) HOT

Fig. 20. Time trends observed at the (A) BATS, (B) ESTOC and (C) HOT stations. The temperature, salinity, alkalinity and TCO$_2$ data for the BATS site are provided by N. Bates (Bates et al., 2012); the temperature, salinity, alkalinity and pH data for the ESTOC site by M. Gonzalez-Davila (Gonzalez-Davila and Santana-Casiano, 2009); and the temperature, salinity, alkalinity, and TCO$_2$ data for the HOT program are from its website (Fujieki et al., 2012, <hahana.soest.hawaii.edu/hot/hot-dogs/bextraction.html hot-jgofs.html>). The pCO$_2$, pH and Ω values are computed using the equilibrium carbonate chemistry model described in Section 2 of this paper, so that these values are consistent with the global values presented in this paper. The red lines indicate the linear regression line, $Y = aX + b$, and the uncertainty is computed using $\pm \sigma^2/(\Sigma Xi^2 - N \,(\text{mean } Xi)^2$, where σ^2 is $\{\Sigma(Yi - aXi - b)^2\}/(N-2)$, N is the number of years, Xi is decimal year, and a and b are the slope and intercept of regression line. The mean rates of change are summarized in Table 2.

Fig. 21. (A) The 2002-2012 time-series observations of SST, pH, CO$_2$,TCO$_2$,TALK, PO$_4$, Ωcalcite and Ωaragonite in the surface water in the two selected areas in the Drake Passage, Southern Ocean, which are oriented in the general direction of the mean flow of ACC and the Antarctic Polar Front. The decadal mean rates of change are based on the regression lines (heavy red lines), and are listed in Table 4. (B) Map shows the location of the samples with the background of climatological mean SST. Area 1 (outlined by pink lines) is located just south of the sub-Antarctic Front (SAF) within ACC, and Area 4 is located south of the Antarctic Polar Front.

(A)
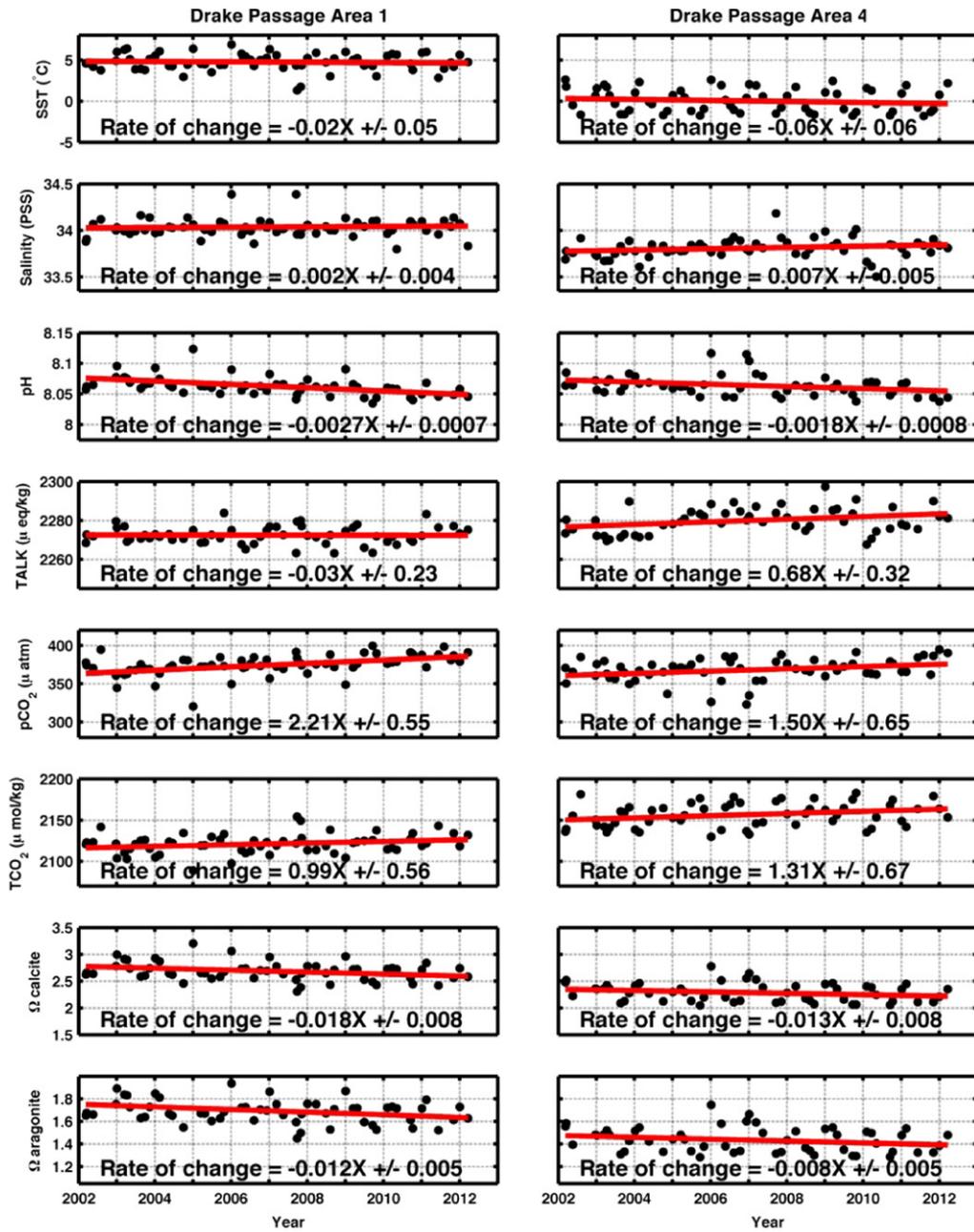
(B)
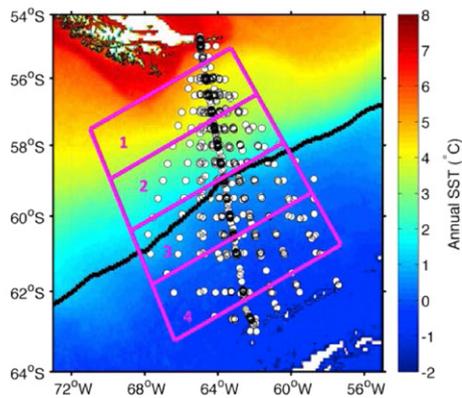
Table 3
Salinity effect on the mean decadal rate for TA and TCO$_2$. Salinity is in PSS, TA is in µeq kg^{-1}, and TCO$_2$ is in µmol kg^{-1}; and all the rates are expressed in per decade. The uncertainty for the mean TA/TCO$_2$ ratio represents a combined uncertainty for the mean TA and TCO$_2$ values; and the uncertainty for its rate of change reflects only the uncertainties in the rates of change in TA and TCO$_2$. The possible causes for the changes are listed in the last column.

	MEAN	OBS. RATES (dcade^{-1})	SALINITY EFFECTS (decade^{-1})	POSSIBLE CAUSES FOR TA AND TCO$_2$ CHANGES
BATS				
Sal	36.6 ± 0.2	0.055 ± 0.01		
TA	2389 ± 11	4.7 ± 0.7	3.6 ± 0.7	Salinity increase
TCO$_2$	2047 ± 21	15.5 ± 1.2	3.1 ± 0.6	Air CO$_2$ uptake; Salinity increase
TA/TCO$_2$	1.167 ± 0.013	-0.0065 ± 0.0008		
ESTOC				
Sal	36.8 ± 0.1	-0.01 ± 0.02		
TA	2410 ± 6	-0.95 ± 1.2	-0.65 ± 1.3	Salinity decrease
TCO$_2$	2099 ± 8	9.5 ± 1.4	-0.57 ± 1.1	Air CO$_2$ uptake; Bio production increase.
TA/TCO$_2$	1.148 ± 0.005	-0.006 ± 0.001		
HOT				
Sal	35.1 ± 0.2	0.13 ± 0.02		
TA	2308 ± 14	9.5 ± 1.3	8.5 ± 1.3	Salinity increase
TCO$_2$	1978 ± 17	17.5 ± 1.3	7.3 ± 1.1	Air CO$_2$ uptake; Salinity increase
TA/TCO$_2$	1.167 ± 0.012	-0.006 ± 0.001		
Drake 1				
Sal	34.03 ± 0.10	0.02 ± 0.04		
TA	2272 ± 5	-0.5 ± 2.3	1.2 ± 2.9	No change
TCO$_2$	2121 ± 12	9.9 ± 5.6	1.1 ± 2.7	Air CO$_2$ uptake
TA/TCO$_2$	1.071 ± 0.006	-0.005 ± 0.003		
Drake 4				
Sal	33.81 ± 0.11	0.07 ± 0.05		
TA	2280 ± 7	6.0 ± 3.1	4.7 ± 3.2	Salinity increase
TCO$_2$	2156 ± 15	13.1 ± 6.7	4.4 ± 3.0	Air CO$_2$ uptake; Salinity increase
TA/TCO$_2$	1.058 ± 0.006	-0.004 ± 0.003		

and frontal meandering, they are not used for this analysis. The decadal mean trends are listed in Table 2.

We find that the Antarctic Circumpolar Current north of the Polar Front in the Drake Passage (Drake Area 1, Table 2) exhibits pCO$_2$ and pH time-trends which are similar to those of the subtropical waters, although the rates can be estimated only with large uncertainty because of the large seasonal amplitude and shorter duration of observations (10 years). The pH change for the sub-Antarctic Zone (SAZ, 45 °S-53 °S) estimated by Midorikawa et al. (2012) are somewhat lower than the others, but it may be biased because it is based only on the summertime observations made during 8 cruises in 1969-2003. Therefore, a large portion of the global oceans including the subtropical, subarctic and sub-Antarctic zones appears to have nearly uniform mean decadal rate of change for pH of about -0.02 pH decade^{-1} and pCO$_2$ of about 19 µatm decade^{-1}, which is similar to the mean atmospheric pCO$_2$ increase rate of about 19 µatm decade^{-1} observed during the 20 year period 1993-2012. This suggests that the uptake of atmospheric CO$_2$ plays the major role in governing the pCO$_2$ and TCO$_2$ of the mixed layer waters of the global ocean.

In contrast, the cold Antarctic Polar Water south of the Polar Front (Drake Zone 4, Table 2 and Fig. 21) shows somewhat smaller changes in pCO$_2$ and pH, albeit they overlap with the Zone 1 trends within the large uncertainties. It appears that the Polar Water is more influenced by regional processes such as rapid vertical mixing associated with the Antarctic environment.

6.2. Regional Differences in Time Trend and Drivers

6.2.1. Salinity and the E-P Effect

While the rates of change in pCO$_2$ and pH are similar over the large areas of the oceans, the rates of change for the drivers differ regionally as summarized in Table 2. The effects of salinity changes on TA and

TCO$_2$ will be examined first. Assuming that salinity is changed only by the E-P balance, the changes in TA and TCO$_2$ due to salinity changes are computed as proportional to the salinity, and these values are listed in Table 3 for comparison with the observed rates. At the BATS site, TA and TCO$_2$ should increase at 3.6 ± 0.7 µeq kg^{-1} and 3.1 ± 0.6 µmol kg^{-1} decade^{-1} respectively in response to the observed salinity increase rate of 0.055 PSS decade^{-1}. The close agreement of the estimated increase in TA with the observed rate of 4.7 ± 0.7 µeq kg^{-1} decade^{-1} suggests that the increase in TA is attributed mostly to E-P change. On the other hand, the observed increase in TCO$_2$ of 15.5 ± 1.2 µmol kg^{-1} decade^{-1} is nearly 3 times as large as the salinity-based estimate, suggesting that other processes, such as the sea-air CO$_2$ exchange which affects TCO$_2$ but not TA, are responsible. An increase in TCO$_2$ of about 11 µmol kg^{-1} is expected in response to a decadal atmospheric CO$_2$ increase of 19 µatm when sea-air CO$_2$ equilibrium is assumed. The total increase in TCO$_2$ estimated for the sea-air flux and salinity increase is 14 µmol kg^{-1}, which is consistent with the observed value. The uptake of atmospheric CO$_2$ by seawater is, therefore, the predominant cause for the decadal mean increase of TCO$_2$ in surface water with negligible changes in the carbon balance between the net community production and seasonal upwelling of subsurface waters.

At the HOT site, the situation is similar to BATS: the observed TA rate is consistent with the salinity increase, while the TCO$_2$ rate is more than twice as high as the salinity effect (Table 3). The TCO$_2$ rate is governed by the CO$_2$ uptake from the air and E-P change.

At ESTOC, the observed small decrease in TA is accounted for by the salinity decrease (Table 3), whereas the observed increase rate for TCO$_2$ of 9.5 µmol kg^{-1} is less than that expected for the atmospheric CO$_2$ input rate. This may be attributed to an increase in the biological production of organic carbon.

At the Drake Area 1, the salinity and TA remain nearly unchanged (0.02 ± 0.04 PSS decade^{-1} and 1.2 ± 2.9 µeq kg^{-1} respectively). On the

Table 4

Decadal mean values and seasonal amplitudes of surface water properties observed and calculated for the BATS, ESTOC, HOT and Drake Passage sites. In the OBSERVED columns, the values with "*" indicate the computed values from the observations using the carbon chemistry model. The mean peak-to-peak SEASONAL AMPLITUDE is computed as the July-August-September mean minus the January-February-March mean value, and hence its sign indicates the phase relationships. When the seasonal phase cannot be clearly identified, it is marked "irregular"; and the corresponding boxes in the CALCULATED SEASONAL AMPLITUDE columns are marked with"?". The $\pm$ values for the OBSERVED columns are expressed by one standard deviation (σ) for the time-series mean and the peak-to-peak amplitude, and reflect the interannual variability. The $\pm$ values without the parentheses in the CALCULATED columns are computed by propagating the one-sigma interannual variability for the observed amplitude; and the $\pm$ values in the parentheses indicate the uncertainties due to the errors in the effects of the forcing parameters on the seasonal amplitude (Table 5). **Bold-faced numbers** are the sum of the calculated contributions from the four forcings, and are to be compared with the observed amplitude for corresponding property.

	——————OBSERVED——————		———————————— CALCULATED SEASONAL AMPLITUDE ————————————			
BATS **(N. Atlantic)**	ANNUAL MEAN	SEASONAL AMPLITUDE	Δ pCO$_2$ (μatm)	Δ pH	Δ Ωaragonite	Δ Ωcalcite
Temp (°C)	23 ± 3	+8.6 ± 0.8	+137 ± 12	−0.14 ± 0.01	+0.10 ± 0.01	+0.10 ± 0.01
Salinity (PSS)	36.6 ± 0.2	−0.4 ± 0.2	−4 ± 2	+0.005 ± 0.003	+0.015 ± 0.008	+0.03 ± 0.01
TA (μeq kg^{-1})	2389 ± 11	−28 ± 13	+36 ± 18	−0.05 ± 0.02	−0.3 ± 0.1	−0.5 ± 0.2
TCO$_2$ (μmol kg^{-1})	2047 ± 21	−47 ± 17	−79 ± 28	+0.09 ± 0.03	+0.5 ± 0.2	+0.7 ± 0.3
pCO$_2$ (μatm)	343 ± 34*	+92 ± 18	**+91 ± 35 (± 5)**	–	–	–
pH (total H$^+$)	8.11 ± 0.04*	−0.10 ± 0.02	–	**−0.09 ± 0.04 (± 0.01)**	–	–
Ωaragonite	3.7 ± 0.2*	+0.5 ± 0.1	–	–	**+0.3 ± 0.2 (± 0.03)**	–
Ωcalcite	5.7 ± 0.3*	+0.7 ± 0.2	–	–	–	**+0.4 ± 0.3 (± 0.06)**
ESTOC **(N. Atlantic)**						
Temp (°C)	21 ± 2	+5.0 ± 0.8	+82 ± 12	−0.08 ± 0.01	+0.06 ± 0.01	+0.06 ± 0.01
Salinity (PSS)	36.8 ± 0.1	+0.24 ± 0.08	+2.4 ± 0.8	−0.003 ± 0.001	−0.009 ± 0.002	−0.016 ± 0.005
TA (μeq kg^{-1})	2410 ± 6	+16 ± 4	−21 ± 6	+0.027 ± 0.007	+0.16 ± 0.04	+0.26 ± 0.06
TCO$_2$ (μmol kg^{-1})	2099 ± 8*	−19 ± 6	−33 ± 10	+0.04 ± 0.01	+0.18 ± 0.04	+0.29 ± 0.09
pCO$_2$ (μatm)	367 ± 21*	+52 ± 8	**+30 ± 17 (± 2)**	–	–	–
pH (total H$^+$)	8.09 ± 0.02	−0.05 ± 0.01	–	**−0.02 ± 0.02 (± 0.01)**	–	–
Ωaragonite	3.3 ± 0.1*	+0.31 ± 0.05	–	–	**+0.39 ± 0.06 (± 0.02)**	–
Ωcalcite	5.1 ± 0.3*	+0.40 ± 0.08	–	–	–	**+0.6 ± 0.1 (± 0.03)**
HOT **(N. Pacific)**						
Temp (°C)	25 ± 1	+3.2 ± 0.7	+47 ± 10	−0.05 ± 0.01	+0.04 ± 0.01	+0.04 ± 0.01
Salinity (PSS)	35.1 ± 0.2	irregular	?	?	?	?
TA (μeq kg^{-1})	2308 ± 14	irregular	?	?	?	?
TCO$_2$ (μmol kg^{-1})	1978 ± 17	irregular	?	?	?	?
pCO$_2$ (μatm)	347 ± 17*	+34 ± 12	**+47 ± 10 (± 0.2)**	–	–	–
pH (total H$^+$)	8.09 ± 0.02*	−0.04 ± 0.01	–	**−0.05 ± 0.01(± 0.003)**	–	–
Ωaragonite	3.7 ± 0.1*	+0.25 ± 0.08	–	–	**+0.04 ± 0.01(± 0.006)**	–
Ωcalcite	5.6 ± 0.2*	+0.3 ± 0.1	–	–	–	**+0.03 ± 0.01 (± 0.003)**

	——————OBSERVED——————		———————————— CALCULATED SEASONAL AMPLITUDE ————————————			
Drake Area 1 **(S. Ocean)**	ANNUAL MEAN	SEASONAL AMPLITUDE	Δ pCO$_2$ (μatm)	Δ pH	Δ Ωaragonite	Δ Ωcalcite
Temp (°C)	4.8 ± 1.1	−1.6 ± 0.6	−25 ± 9	+0.026 ± 0.009	−0.02 ± 0.01	−0.02 ± 0.01
Salinity (PSS)	34.03 ± 0.10	+0.09 ± 0.11	+1 ± 1	−0.001 ± 0.001	0.00 ± 0.00	0.00 ± 0.00
TA (μeq kg^{-1})	2272 ± 5*	−5 ± 5	+9 ± 9	−0.009 ± 0.009	−0.05 ± 0.05	−0.08 ± 0.08
TCO$_2$ (μmol kg^{-1})	2121 ± 12	+13 ± 10	+29 ± 20	−0.026 ± 0.018	−0.13 ± 0.09	−0.20 ± 0.14
pCO$_2$ (μatm)	375 ± 13	+20 ± 23	**+13 ± 24 (± 4)**	–	–	–
pH (total H$^+$)	8.06 ± 0.02*	−0.02 ± 0.01	–	**−0.01 ± 0.02 (± 0.003)**	–	–
Ωaragonite	1.7 ± 0.1*	−0.18 ± 0.05	–	–	**−0.20 ± 0.10 (± 0.01)**	–
Ωcalcite	2.7 ± 0.3*	−0.27 ± 0.08	–	–	–	**−0.30 ± 0.16 (± 0.03)**
Drake Area 4 **(S. Ocean)**						
Temp (°C)	0.2 ± 1.5	−3.4 ± 0.5	−51 ± 8	+0.054 ± 0.008	−0.04 ± 0.01	−0.03 ± 0.01
Salinity (PSS)	33.81 ± 0.11	+0.14 ± 0.14	+1 ± 1	−0.002 ± 0.002	0.00 ± 0.00	0.00 ± 0.00
TA (μeq kg^{-1})	2280 ± 7*	+3 ± 9	−6 ± 15	+0.006 ± 0.016	+0.03 ± 0.08	+0.05 ± 0.14
TCO$_2$ (μmol kg^{-1})	2156 ± 15	+28 ± 12	+58 ± 24	−0.054 ± 0.022	−0.27 ± 0.11	−0.43 ± 0.18
pCO$_2$ (μatm)	368 ± 15	+16 ± 18	**+3 ± 30 (±4)**	–	–	–
pH (total H$^+$)	8.07 ± 0.02*	−0.02 ± 0.01	–	**0.00 ± 0.03 (± 0.003)**	–	–
Ωaragonite	1.4 ± 0.2*	−0.13 ± 0.07	–	–	**−0.28 ± 0.14 (± 0.01)**	–
Ωcalcite	2.3 ± 0.3*	−0.36 ± 0.14	–	–	–	**−0.41 ± 0.22 (± 0.02)**

other hand, the observed TCO$_2$ increase is 9.9 ± 5.6 μmol kg^{-1} decade^{-1}, which is nearly ten times as large as the salinity induced change of 1.1 ± 2.7 μmol kg^{-1}, and suggests that it is due primarily to the uptake of atmospheric CO$_2$. At the Drake Area 4 site, the observed rates for TA in the Polar Water (6.0 ± 3.1 μeq kg^{-1} decade^{-1}) is consistent with the rate of 4.7 ± 3.2 μeq kg^{-1} decade^{-1} due to salinity change of 0.07 ± 0.05, whereas TCO$_2$ increases at a rate (13.1 ± 6.7 μmol kg^{-1} decade^{-1}) which is three times as fast as that from salinity change (4.4 ± 3.0 μmol kg^{-1} decade^{-1}). The observed rate is somewhat faster than that for atmospheric

CO$_2$ uptake (about 11 μmol kg^{-1} decade^{-1}), and suggests a combination of the atmospheric and salinity effects.

6.2.2. The Effect of TA/TCO$_2$ ratio

The Ω values for aragonite and calcite for the subtropical and ACC waters decrease at a mean rate of about -0.1 decade^{-1} and -0.15 decade^{-1} respectively, whereas they decrease at about 30% slower rate in the Polar Water (Drake Area 4) in the Southern Ocean (Table 2). This may be attributed primarily to the high sensitivity of CO$_3^=$ and Ω

to the TA/TCO_2 ratio. For an increase of 0.1 in TA/TCO_2 ratio, $CO_3^=$ increases by 110 µmol kg^{-1}, Ωaragonite by 1.6 and Ωcalcite by 2.5, while these sensitivities are nearly independent of temperature. The pH is sensitive to change in temperature as well as the TA/TCO_2 ratio: its sensitivity, $\Delta pH/\Delta(TA/TCO_2)$, is 0.35 pH per 0.1 (TA/TCO_2). In these waters, the TA/TCO_2 ratio decreases in a range of 0.005 to 0.0065 per decade (Table 3) because of the rapid increase in TCO_2. Using the sensitivities given above, we estimate that Ω should decrease by -0.1 for aragonite and -0.15 for calcite, which are consistent with the observed values (Table 2). In the Polar Water (Drake Area 4), TA/TCO_2 decreases at somewhat slower rate, and hence the rates of change for Ωs are correspondingly slower.

The carbonate chemistry of the oceans depends sensitively on the TA/TCO_2 ratio. While TA and TCO_2 are both regulated by common physical and biological processes, TCO_2 is changed additionally by the sea-air transfer of CO_2. Although the present rate of change of TA/TCO_2 is small (~0.5% per decade, Table 3), the TCO_2 should increase by the uptake of rapidly increasing atmospheric CO_2 and may lower the ratio significantly in a time scale of several decades if TA remains unchanged. We must pay closer attention to changes in TA as well as TCO_2 for the improved prediction of the future ocean CO_2 uptake rate, as pointed out by Lenton et al. (2012).

6.3. Seasonal Changes

The decadal mean values and mean seasonal amplitude of surface water properties at the five time-series sites, which are computed using the data presented in Figs. 20 and 21, are summarized in Table 4. The seasonal amplitude is given as the July-August-September mean value minus the January-February-March mean value. The ± values in seasonal amplitudes indicate the one-sigma interannual variability. At the three northern subtropical sites, the seasonal amplitudes for the SST, TA and pCO_2 are positive (i. e. the summer values are higher than the winter values), whereas TCO_2 and pH are negative (i. e. summer values are lower). The opposing signs of amplitude values indicate that the seasonal changes are out of phase by about 6 months.

The significance of the seasonal amplitude may be visualized in the context of the secular rates of change (see Table 2). At these mean rates, the secular change would exceed the seasonal amplitude in 40 to 50 years at BATS and 20 to 30 years at ESTOC and HOT sites. This means that, after these periods, the marine organisms will be exposed to entirely new conditions that are beyond the seasonal variability of their previous exposures. The longer time scale at BATS is due primarily to the larger seasonal amplitudes in temperature and TCO_2. For the Drake Passage sites, the time scale cannot be estimated with any better

accuracy than the range of 20 to 250 years because of the large uncertainty in the estimated rate of change.

6.3.1. Effect of Temperature

At the three subtropical sites (Table 4), the sign for the seasonal amplitude of pH is negative, whereas that for Ω is positive. This means that, while the water becomes more acidic (lower pH) from winter to summer, the degree of $CaCO_3$ saturation (Ω) increases, which at first appears counter intuitive. The main reason is the effect of temperature on the dissociation constants of carbonic acid in seawater. Note that:

$$K_2'/K_1' = [H_2CO_3][CO_3^=]/[HCO_3^-]^2 \approx 10^{-3}, \text{ and } [H_2CO_3] = Ko' \cdot pCO_2,$$

where Ko' is the solubility of CO_2 in seawater, and K_1' and K_2' are the first and second dissociation constants of carbonic acid. K_2' increases 1.5 times faster than K_1' with increasing temperature. Since the K_2'/K_1' ratio increases with increasing temperature, the $[H_2CO_3][CO_3^=]$ should increase, and $[HCO_3^-]$ should decrease to conserve the charge and mass balance. An increase in pCO_2 demands an increase in H^+ (lower pH) for converting HCO_3^- to H_2CO_3. However, as a result of faster increase in K_2', $CO_3^=$ should increase causing Ω to increase. The decrease in the solubility product of $CaCO_3$, Ksp', in warmer waters also contributes to the increase in Ω. This explanation is consistent with the chemical model used in this paper as well as in computer programs used commonly by other investigators.

In contrast to the northern subtropical sites, at the high southern latitude Drake Passage sites the seasonal changes of TCO_2 and pCO_2 both have positive signs, whereas SST, pH and Ω's have negative signs (note that the signs are reversed in the southern hemisphere). This means that pCO_2 is decreased from winter to summer by biological drawdown of TCO_2, while the small temperature increase in summer partially counteracts the TCO_2 effect. Here, the seasonal warming of water plays a minor role, and the biological drawdown of TCO_2 and the resulting increase in the TA/TCO_2 ratio are the dominant cause for the increase in pH and the degree of $CaCO_3$ saturation from winter to summer.

6.3.2. Drivers for Seasonal Change

In this section, we discuss the relative importance of the four environmental drivers, temperature (T), TCO_2, TA and Salinity (Sal) contributing to the seasonal amplitude of the four chemical properties "X" ($= pCO_2$, pH, Ωaragonite, or Ωcalcite). The changes in a property "X" may be expressed in terms of the four drivers by:

$$\Delta X = (\partial X/\partial T)\,\Delta T + (\partial X/\partial TCO_2)\,\Delta TCO_2 + (\partial X/\partial TA)\,\Delta TA$$
$$+ (\partial X/\partial Sal)\,\Delta Sal... \quad\quad\quad (1)$$

Table 5

Effects of temperature, TCO_2, TA and salinity on seawater pCO_2, pH and Ωs. These values are estimated using the chemical model described in Section 2, and are used in Eq. (1) for estimating the effect of each environmental driver on the pH, Ωaragonite and Ωcalcite. The magnitude for seasonal amplitude is obtained by multiplying the peak-to-peak amplitude values (ΔT, ΔTCO_2, ΔTA and ΔSal in Table 4) to the corresponding sensitivity values in this table. The sensitivities for some parameters are approximated by a constant, whereas some others are expressed as a function of the mean values ($\bar{p}CO_2$, $\bar{\Omega}$aragonite and $\bar{\Omega}$calcite) which are listed in Table 4, and those for pCO_2 are expressed by the equations listed in (a), (b) and (c) below.

		———————————————— X in Equation (1) ————————————————			
		pCO_2 (µatm)	pH (total H^+ scale)	Ωaragonite (ICP/Ksp')	Ωcalcite (ICP/Ksp')
$\partial X/\partial T$	$°C^{-1}$	(a)	-0.016 ± 0.001	$+0.012 \pm 0.002$	$+0.010 \pm 0.001$
$\partial X/\partial TCO_2$	$(µmol/kg)^{-1}$	(b)	-0.0019 ± 0.0001	-0.0095 ± 0.0005	-0.015 ± 0.001
$\partial X/\partial TA$	$(µeq/kg)^{-1}$	(c)	$+0.0018 \pm 0.0001$	$+0.0095 \pm 0.0005$	$+0.016 \pm 0.001$
$\partial X/\partial Sal$	$(PSS)^{-1}$	$0.026(\pm 0.002) \cdot pCO_2$	-0.0125 ± 0.0005	$-0.010(\pm 0.002) \cdot \bar{\Omega}$arag	$-0.012(\pm 0.002) \cdot \bar{\Omega}$calcite

(a) $\Delta pCO_2 = (\partial pCO_2/\partial T)\,\Delta T = 2\,(\bar{p}CO_2)\,[Exp\,(0.0423(\pm 0.0002)\,\Delta T/2) - 1]$, where $\bar{p}CO_2$ is the mean pCO_2 value in Table 4.

(b) $(\partial pCO_2/\partial TCO_2) = \gamma_{CO2}\,(\bar{p}CO_2/\bar{T}CO_2)$, where γ_{CO2} is the Revelle factor for CO_2, $(\partial \ln pCO_2/\partial \ln TCO_2)$, and is set at 10 ± 0.5 for the BATS, ESTOC and HOT sites, and 12 ± 0.5 for the Drake B and C sites.

(c) $(\partial pCO_2/\partial TA) = \gamma_{Alk}\,(\bar{p}CO_2/\bar{T}A)$, where γ_{Alk} is the Revelle factor for TA, $(\partial \ln pCO_2/\partial \ln TA)$, and is set at -9 ± 0.5 for the BATS, ESTOC and HOT sites, and -11 ± 0.5 for the Drake B and C sites.

where ΔT, ΔTCO_2, ΔTA and ΔSal are the peak-to-peak seasonal amplitudes listed in Table 4. The observed seasonal changes in pCO_2, pH and Ω will be analyzed on the basis of this equation. The partial differential terms for each of the four drivers are estimated using the chemical model described in Section 2, and are listed in Table 5. TCO_2 and TA are affected by biological activities, vertical/lateral water mixing and E-P of water and, in addition, TCO_2 is affected by the sea-air gas exchange. The $(\partial X/\partial Sal)$ term represents the effects of salinity on the dissociation constants as well as the change of boric acid proportional to salinity. The effects of each driver on pCO_2, pH and Ω's computed using Eq. (1) are listed in the four columns on the right half of Table 4, and the sum of the effects of the four drivers is shown in bold-faced numbers for comparison with the observed amplitude. The $\pm$ values without parentheses represent the interannual variability (one sigma), and those in the parentheses, which are much smaller than the former, are the uncertainties resulting from the sensitivity approximations (Table 5) used for the seasonal amplitude.

Of the five time-series observations, BATS is the most extensive and complete set. The calculated seasonal amplitudes for pCO_2, pH and Ω's are in agreement with the observations well within the respective uncertainties (Table 4). Temperature has the most dominant effect on the seasonal amplitude of pCO_2 (+ 137 µatm). This is partially compensated by the lowering effect of the TCO_2 reduction (-79 µatm), although this is further counteracted by the increasing effect on pCO_2 of the reduction of TA (+ 36 µatm). Salinity contribution (-4) is small. The sum of these calculated effects of + 91 µatm (= 137 - 79 + 36 - 4) is in good agreement with the observed mean pCO_2 amplitude of 92 µatm. The seasonal pH change is also regulated primarily by temperature (-0.14), while it is partially modulated by the effects of changes in TCO_2 (+0.09) and TA (-0.05). In contrast to pCO_2 and pH, the Ω values are regulated primarily by changes in TCO_2 and TA, which have opposing effects cancelling partially each other. The overall calculated change of -0.09 is in good agreement with the observed mean value of -0.10. The calculated amplitudes for Ωaragonite and Ωcalcite are found to be consistent with the observed values.

At the ESTOC site, temperature plays the dominant role in regulating pCO_2 and pH as observed at BATS. However, the calculated ΔpCO_2 (+30 ± 17 µatm) and ΔpH (-0.02 ± 0.02 pH) values are nearly one half the respective observations (+ 52 ± 8 µatm and -0.05 ± 0.01 pH), although these values barely overlap within the range of interannual variability. The causes for these discrepancies are not clear. However, the estimated seasonal amplitude for TA and salinity may be biased because of the irregular changes without a clear seasonal trend during the 1996-2000 and 2007-2010 periods (see Fig. 20-B). This may have affected the amplitudes of TCO_2 and pCO_2, which are computed using the TA data. On the other hand, the calculated Ω values are consistent with the observed values. As observed at BATS, the seasonal amplitude for Ω's is primarily regulated by changes in TA and TCO_2 rather than temperature.

At the HOT site (Fig. 20-C), the regular periodic seasonal changes for the salinity, TA and TCO_2 are obscured by natural perturbations caused by changes in E-P and lateral mixing (Dore et al., 2003; Keeling et al., 2004). The seasonal pCO_2 trends may have been affected somewhat due to the transition of the Pacific Decadal Oscillation to the negative phase around the mid-2000's (Fay and McKinley, 2013). Therefore, only the temperature effects can be assessed without the effects of TA and TCO_2. The calculated amplitudes for pCO_2 and pH based only on the temperature effect are found to be consistent with the observations, because temperature is the primary driver for these properties. On the other hand, the calculated Ω values are nearly an order of magnitude smaller than the observed values, because they are mainly driven by the TA/TCO_2 change which could not be determined due to their irregular seasonal behavior.

In the Antarctic Circumpolar Current sampled across the Drake Passage (Drake Area 1), the computed seasonal amplitudes for the four parameters are consistent with the measured values. Since the changes

in TCO_2 and TA are out of phase, the effects of TCO_2 and TA on pCO_2 and pH reinforce each other and their combined effects are nearly twice as large as the temperature effect. However, the effect of TCO_2 is nearly three times as large as that of TA, and is the most important forcing factor, although the temperature effect partially cancels the effects of TCO_2 and TA. The Ω values are regulated primarily by TA/TCO_2, but the TCO_2 effect is more than twice as large as the effect of TA. In the colder Polar Water (Drake Area 4), the observed seasonal amplitudes are broadly consistent with the calculated values, and are also similar to those for Drake Area 1. Ω values are governed primarily by TCO_2, and the seasonal amplitude of pCO_2 and pH are small because of the near cancellation by the opposing effects of temperature and TCO_2. It should be noted that in these nutrient-rich subpolar waters, the seasonal amplitudes of pCO_2, pH and Ω's depend primarily on TCO_2 and TA, which are regulated largely by biological processes and deep water upwelling, whereas, in oligotrophic waters of the BATS, ESTOC and HOT sites, they depend mainly on the seasonal temperature variation.

7. Summary and conclusion

1) A database for the alkalinity (TA), pCO_2 and the concentrations of total CO_2 (TCO_2) and nutrients in the surface ocean waters (depths < 50 meters) over the global oceans is assembled by building upon the data synthesis of the GLODAP database (Key et al., 2004) supplemented with the TCO_2-TA pairs from the CARINA program (Tanhua et al., 2009; Key et al., 2010) and pCO_2 and TCO_2 data from the LDEO database. Coastal water data are not included in the assembled database.

2) The global distribution of surface water TA is obtained using the linear relationships between potential alkalinity (PALK = TA + NO_3^-) and salinity in 24 ocean regions. Because of the significant interannual variation associated with El Niño events, the equatorial Pacific zone (4°N - 4°S) is not included in the analysis. The seasonal change in TA is found to be small even in subpolar waters where the nutrient concentrations vary seasonally over a wide range due to the net community production. This is attributed to partial cancellation of the effect of seasonal changes in salinity and that of nutrients.

3) The mutual consistency between TA-TCO_2-pCO_2 values used for the computation of the pH and the degree of saturation of $CaCO_3$ is tested and validated successfully using the available observations including the time-series data at the BATS, ESTOC and HOT programs.

4) Using the mean monthly pCO_2 data adjusted to a reference year 2005 and the estimated alkalinity, the climatological mean distributions of pH and the $CaCO_3$ saturation levels in global surface ocean waters (not including the coastal domain) are computed for each month of the year 2005.

5) The calculated pH (the total H^+ scale) in the global open-ocean surface waters ranges from 7.9 to 8.2 in the year 2005. Lower values are located in the upwelling regions in the tropical Pacific and in the Arabian and Bering Seas; and higher values are found in the subpolar and polar waters during the spring-summer months of intense photosynthetic production. The vast areas of subtropical oceans (excluding the Pacific equatorial zone and coastal zone) have seasonally varying pH values ranging from 8.05 during warmer months to 8.15 during colder months. The warm tropical and subtropical waters are supersaturated by a factor of as much as 4.2 with respect to aragonite and 6.3 for calcite, whereas the cold subpolar and polar waters are less supersaturated by a factor of 1.2 for aragonite and 2.0 for calcite because of the lower pH values resulting from greater TCO_2 concentration and lower TA/TCO_2 ratio. Consistent with recent observations (Bates and Mathis, 2009; Bates et al., 2009; Chierici and Fransson, 2009; Robbins et al., 2013), low salinity waters in the western Arctic Ocean are found to be undersaturated with respect to aragonite.

6) Time-series data at the Bermuda (BATS), Hawaii (HOT), northern North Atlantic (Iceland Sea) and Drake Passage (Antarctic

Circumpolar Current) show that, over the extensive global ocean areas (excluding the polar oceans), pH has been declining at a mean rate of about -0.02 pH per decade, and the pCO_2 has been increasing at a rate of 19 µatm per decade. The observed increase rate of oceanic pCO_2 is consistent with the mean increase rate of 19 ppm per decade in atmospheric CO_2 concentrations in the past 20 years. This suggests that the global oceans are being acidified primarily in response to the atmospheric CO_2 increase. Changes in other physical and biological processes that have occurred to-date in local waters do not appear to detectably modulate the global mean acidification rate as yet.

7) The seasonal changes in pCO_2, pH and Ω's are quantitatively analyzed. At the warm oligotrophic sites (BATS, ESTOC and HOT), temperature is the primary driver for the seasonal variability for pCO_2, pH and $CaCO_3$ saturation. On the other hand, in the sub-Antarctic and Antarctic waters, TCO_2 and temperature are the primary drivers, but their effects have opposite signs and partially cancel each other.

8) The two important environmental properties in surface oceans, pH and the degree of saturation of $CaCO_3$, depend primarily on TCO_2, TA and temperature. While TA and TCO_2 are both regulated by common physical and biological processes, TCO_2 is changed additionally by the sea-air transfer of CO_2. Closer attention should be paid to TA as well as TCO_2 for the improved prediction of the future course of ocean's role in the global carbon cycle.

Acknowledgments

References

Anderson, L.G., Jutterstrom, S., Kaltin, S., Jones, P.E., Bjork, G., 2004. Variability in river runoff distribution in the Eurasian Basin of the Arctic Ocean. J. Geophys. Res. 109. http://dx.doi.org/10.1029/2003JC001773 (C01016).

Antonov, J.I., Seidov, D., Boyer, T.P., Locarnini, R.A., Mishonov, A.V., Garcia, H.E., Baranova, O.K., Zweng, M.M., Johnson, D.R., 2010. World Ocean Atlas 2009. In: Levitus, S. (Ed.), NOAA Atlas NESDIS 69. Salinity, vol. 2. U.S. Government Printing Office, Washington, D.C. (184 pp., http://www.nodc.noaa.gov/OC5/WOA09/woa09data.html).

Bakker, D.C.E., et al., 2014. An update to the surface ocean CO_2 atlas (SOCAT version 2). Earth Syst. Sci. Data 6, 69–90. http://dx.doi.org/10.5194/essd-6-69-2014 (www.earth-sys-sci-data.net/6/69/2014/).

Balch, W.M., Gordon, H.R., Bowler, B.C., Drapeau, D.T., Booth, E.S., 2005. Calcium carbonate budgets in the surface global ocean based on MODIS data. J. Geophys. Res. 110. http://dx.doi.org/10.1029/2004JC002560 (C07001).

Bates, N.R., Michaels, A.F., Knap, A.H., 1996. Seasonal and interannual variability of oceanic carbon dioxide species at the US JGOFS Bermuda Atlantic Time-series Study (BATS) site. Deep-Sea Res. II 43, 347–383. http://dx.doi.org/10.1016/0967-0645(95)00093-3 (Corrigendum: 43, 1435–1435, 1996).

Bates, N.R., 2001. Interannual variability of oceanic CO_2 and biogeochemical properties in the Western North Atlantic subtropical gyre. Deep-Sea Res. II 48 (8–9), 1507–1528.

Bates, N.R., 2007. Interannual variability of the oceanic CO_2 sink on the subtropical gyre of the North Atlantic Ocean over the last 2 decades. J. Geophys. Res. 112, 2007. http://dx.doi.org/10.1029/2006JC003759.

Bates, N.R., Mathis, J.T., 2009. The Arctic Ocean marine carbon cycle: evaluation of air-sea CO_2 exchanges, ocean acidification impacts and potential feedbacks. Biogeosciences 6, 2433–2459 (www.biogeosciences.net/6/2433/2009/).

Bates, N.R., Mathis, J.T., Cooper, L.W., 2009. Ocean acidification and biologically induced seasonality of carbonate mineral saturation states in the western Arctic Ocean. J. Geophys. Res. 114. http://dx.doi.org/10.1029/2008JC004862,2009 (C11007).

Bates, N.R., Best, M.H.P., Neely, K., Garley, R., Dickson, A.G., Johnson, R.J., 2012. Detecting anthropogenic carbon dioxide uptake and ocean acidification in the North Atlantic Ocean. Biogeosciences 9, 2509–2522. http://dx.doi.org/10.5194/bg-9-2509-2012 (www.biogeosciences.net/9/2509/2012/).

Brewer, P.G., Goldman, J.C., 1976. Alkalinity changes generated by phytoplankton growth. Limnol. Oceanogr. 21, 108–117.

Chen, C.-T.A., Pytkowicz, R.M., Olson, E.J., 1982. Evaluation of the calcium problem in the South Pacific. Geochem. J. 16, 1–10.

Chierici, N., Fransson, A., 2009. Calcium carbonate saturation in the surface water of the Arctic Ocean: undersaturation in freshwater influenced shelves. Biogeosci. Discuss. 6, 4963–4991.

Conkright, M., Levitus, S., Boyer, T., 1994. World Ocean Atlas, 1994: Volume 1, Nutrients. NOAA Atlas NESDIS 1. National Oceanic and Atmospheric Administration, Washington, D. C (150 pp.).

Cross, J.N., Mathis, J.T., Bates, N., 2012. Hydrographic controls of net community production and total organic carbon distributions in the eastern Bering Sea. Deep-Sea Res. II 65-70, 98–109.

Cross, J.N., Mathis, J.T., Bates, N.R., Byrne, R.H., 2013. Conservative and non-conservative variations of total alkalinity on the southeastern Bering Sea shelf. Mar. Chem. 154, 100–112.

Dickson, A.G., Riley, J.P., 1979-aa. The estimation of acid dissociation constants in seawater media from potentiometric titrations with strong base. I. The ionic product of water (Kw). Mar. Chem. 7, 89–99.

Dickson, A.G., Riley, J.P., 1979-bb. The estimation of acid dissociation constants in seawater media from potentiometric titrations with strong base. II. The dissociation of phosphoric acid. Mar. Chem. 7, 101–109.

Dickson, A.G., 1981. An exact definition of total alkalinity and a procedure for the estimation of alkalinity and total inorganic carbon from titration data. Deep-Sea Res. 28A, 609–623.

Dickson, A.G., 1990. Thermodynamics of the dissociation of boric acid in synthetic seawater from 273.15 to 318.15 K. Deep-Sea Res. 37, 755–766.

Dickson, A.G., 1993. pH buffers for sea water media based on the total hydrogen ion concentration scale. Deep-Sea Res. 40, 107–118.

Dickson, A.G., 2001. Reference materials for oceanic CO_2 measurements. Oceanography 14, 21–22.

Doney, S.C., Fabry, V.J., Feely, R.A., Kleypas, J.A., 2009. Ocean acidification: the other CO_2 problem. Ann. Rev. Mar. Sci. 1, 169–192.

Dore, J.E., Lukas, R., Sadler, D.W., Karl, D.M., 2003. Climate-driven changes to the atmospheric CO_2 sink in the subtropical North Pacific Ocean. Nature 424, 754–757.

Dore, J.E., Lukas, R., Sadler, D.W., Church, M.J., Karl, D.M., 2009. Physical and biogeochemical modulation of ocean acidification in the central North Pacific. PNAS 106, 12235–12240. http://dx.doi.org/10.1073/pnas.0906044106.

Fay, A.R., McKinley, G.A., 2013. Global trends in surface ocean pCO_2 from in situ data. Glob. Biogeochem. Cycles 27. http://dx.doi.org/10.1002/gbc.20051.

Feely, R.A., Boutin, J., Cosca, C.E., Dandonneau, Y., Etcheto, J., Inoue, H., Ishii, M., LeQuere, C., Mackey, D.J., McPhaden, M., Metzl, N., Poisson, A., Wanninkhof, R., 2002. Seasonal and interannual variability of CO_2 in the equatorial Pacific. Deep-Sea Res. II 49, 2443–2469.

Feely, R.A., Doney, S.C., Cooley, S.R., 2009. Ocean acidification: Present conditions and future changes in high-CO_2 world. Oceanography 22, 36–47.

Feely, R.A., Sabine, C.L., Byrne, R.H., Millero, F.J., Dickson, A.G., Wanninkhof, R., Murata, A., Miller, L.A., Greeley, D., 2012. Decadal changes in the aragonite and calcite saturation state of the Pacific Ocean. Glob. Biogeochem. Cycles 26. http://dx.doi.org/10.1029/2011GB004157 (GB3001).

Fujieki, L.A., Santiago-Mandujano, F., Fumar, C., Lukas, R., Church, M., 2012. Hawaii Ocean Time-series. Data Report 21: 2009, November 2012. University of Hawaii, School of Ocean and Earth Science and Technology, 1000 Pope Road, Honolulu, Hawaii, p. 172 (96822, <hahana.soest.hawaii.edu/hot/hot-dogs/bextraction.html>).

Gonzalez-Davila, M., Santana-Casiano, J.M., 2003. Seasonal and interannual variability of sea-surface carbon dioxide species at the European Station for Time Series in the Ocean at the Canary Islands (ESTOC) between 1996-2000. Glob. Biogeochem. Cycles 17 (1076), 2003. http://dx.doi.org/10.1029/2002GB001993.

González-Dávila, M., Santana-Casiano, J.M., González-Dávila, E.F., 2007. Interannual variability of the upper ocean carbon cycle in the northeast Atlantic Ocean. Geophys. Res. Lett. 34. http://dx.doi.org/10.1029/2006GL028145 (L07608).

Gonzalez-Davila, M., Santana-Casiano, J.M., 2009. Sea Surface and atmospheric fCO_2 data measured during the ESTOC Time Series cruises from 1995-2009. http://cdiac.ornl.gov/ftp/oceans/ESTOC_data/ Carbon Dioxide Information Analysis Center, Oak Ridge National Laboratory, US Department of Energy, Oak Ridge, Tennessee. http://dx.doi.org/10.3334/CDIAC/otg.TSM_ESTOC.

González-Dávila, M., Santana-Casiano, J.M., Rueda, M.J., Llinás, O., 2010. The water column distribution of carbonate system variables at the ESTOC site from 1995 to 2004. Biogeosciences 7, 3067–3081. http://dx.doi.org/10.5194/bg-7-3067-2010.

Gruber, N., Gloor, M., Mikaloff Fletcher, S.E., Doney, S.C., Dutkiewicz, S., Follows, M., Gerber, M., Jacobson, A.R., Joos, F., Lindsay, K., Menemenlis, D., Mouchet, A., Müller, S.A., Sarmiento, J.L., Takahashi, T., 2009. Oceanic sources, sinks, and transport of atmospheric CO_2. Glob. Biogeochem. Cycles 23. http://dx.doi.org/10.1029/2008GB003349,2009 (GB1005).

Gruber, N., Hauri, C., Lachkar, Z., Loher, D., Frölicher, T., Plattner, G.-K., 2012. Rapid progression of ocean acidification in the California Current System. Science 337, 220–223.

Hales, B., Takahashi, T., 2004. High-resolution biogeochemical investigation of the Ross Sea, Antarctica, during the AESOPS (U. S.JGOFS) Program. Glob. Biogeochem. Cycles 18 (3). http://dx.doi.org/10.1029/2003GB002165 (GB3006).

Hauri, C., Gruber, N., Vogt, M., Doney, S.C., Feely, R.A., Lachkar, Z., Leinweber, A., McDonnell, A.M.P., Munnich, M., Plattner, G.-K., 2013. Spatiotemporal variability and long-term trends of ocean acidification in the California Current System. Biogeosciences 10, 193–216. http://dx.doi.org/10.5194/bg-10-193-2013.

Keeling, C.D., 1960. The concentration and isotopic abundances of carbon dioxide in the atmosphere. Tellus XII, pp. 200–203.

Keeling, C.D., Brix, H., Gruber, N., 2004. Seasonal and long-term dynamics of the upper ocean carbon cycle at Station ALOHA near Hawaii. Glob. Biogeochem. Cycles 18. http://dx.doi.org/10.1029/2004GB002227 (GB4006).

Key, R.M., Kozyr, A., Sabine, C.L., Lee, K., Wanninkhof, R., Bullister, J.L., Feely, R.A., Millero, F. J., Mordy, C., Peng, T.H., 2004. A global ocean carbon climatology: Results from Global Data Analysis Project (GLODAP). Glob. Biogeochem. Cycles 18 (4) (doi. GB4031 DEC 29 2004).

Key, R.M., Tanhua, T., Olsen, A., Hoppema, M., Jutterstrom, S., Schirnick, C., van Heuven, S., Kozyr, A., Lin, X., Wallace, D.W., Mintrop, L., 2010. The CARINA data synthesis project: introduction and overview. Earth Syst. Sci. Data 2, 105–121 (www.earth-syst-sci-data. net/2/105/2010).

Lee, K., Tong, L.T., Millero, F.J., Sabine, C.L., Dickson, A.G., Goyet, C., Park, G.-H., Wanninkhof, R., Feely, R.A., Key, R.M., 2006. Global relationships of total alkalinity with salinity and temperature in surface watrs of the world's oceans. Geophys. Res. Lett. 33. http://dx.doi.org/10.1029/2006GL27207 (L19605).

Lenton, A., Metzl, N., Takahashi, T., Kuchinke, M., Matear, R.J., Roy, T., Sutherland, S.C., Sweeney, C., Tilbrook, B., 2012. The observed evolution of oceanic pCO_2 and its drivers over the last two decades. Glob. Biogeochem. Cycles 26. http://dx.doi.org/10.1029/ 2011GB004095 (GB2021).

Lueker, T.J., Dickson, A.G., Keeling, C.D., 2000. Ocean pCO_2 calculated from dissolved inorganic carbon, alkalinity and equations K_1 and K_2: validation based on laboratory measurements of CO_2 in gas and seawater at equilibrium. Mar. Chem. 70, 105–119.

Marion, G.M., Millero, F.J., Camoes, M.F., Spitzer, P., Feistel, R., Chen, C.-T.A., 2011. pH of seawater. Mar. Chem. 126, 89–96.

Midorikawa, T., Ishii, M., Saito, S., Sasano, D., Kosugi, N., Motoi, T., Kamiya, H., Nakadate, A., Nemoto, K., Inoue, H.Y., 2010. Decreasing pH trend estimated from 25-yr time series of carbonate parameters in the western North Pacific. Tellus B 62B, 649–659. http:// dx.doi.org/10.1111/j.1600-0889.2010.00474.x.

Midorikawa, T., Inoue, H.Y., Ishii, M., Sasano, D., Kosugi, N., Hashida, G., Nakaoka, S., Suzuki, T., 2012. Decreasing pH trend estimated from 35-year time series of carbonate parameters in the Pacific sector of the Southern Ocean in summer. Deep-Sea Res. I 61, 131–139.

Millero, F.J., Lee, K., Roche, M., 1998. Distribution of alkalinity in the surface waters of the major oceans. Mar. Chem. 60, 111–130.

Moore, J.K., Abbott, M.R., Richman, J.G., 1999. Location and dynamics of the Antarctic Polar Front from satellite sea surface temperature data. J. Geophys. Res. 104 (C2), 3059–3073.

Mucci, A., 1983. The solubility of calcite and aragonite in seawater at various salinities, temperatures and one atmosphere total pressure. Am. J. Sci. 283, 780–799.

NCEP Reanalysis data, 2001. NCEP/NCAR Reanalysis Monthly Means and Other Derived Variables, provided by the NOAA-CIRES Climate Diagnostics Center, Boulder, CO. (http://www.cdc.noaa.gov/cdc/data/ncep.reanalysis.derived.html).

Olafsson, J., Olafsdottir, S.R., Benoit-Cattin, A., Danielsen, M., Arnarson, T.S., Takahashi, T., 2009. Rate of Iceland Sea acidification from time series measurements. Biogeosciences 6, 2661–2668.

Orr, J.C., et al., 2005. Anthropogenic ocean acidification over the twenty-first century and its impact on calcifying organisms. Nature 437, 681–686. http://dx.doi.org/10.1038/ nature04095.

Robbins, L.L., Wynn, J.G., Lisle, J., Yates, K.K., Knorr, P.O., Byrne, R.H., Liu, X., Patsavas, M.C., Azetsu-Scott, K., Takahashi, T., 2013. Baseline monitoring of the Western Arctic Ocean estimates 20% of the Canadian Basin surface waters are undersaturated with respect to aragonite. PLoS ONE 8 (9), 1–15 (e73796).

Santana-Casiano, J.M., González-Dávila, M., Rueda, M.-J., Llinás, O., González-Dávila, E.-F., 2007. The interannual variability of oceanic CO_2 parameters in the northeast Atlantic subtropical gyre at the ESTOC site. Glob. Biogeochem. Cycles 21. http://dx.doi.org/10. 1029/2006GB002788 (GB1015).

Sjorberg, S., Nordin, N., Ingri, N., 1981. Equilibrium and structural studies of silicon(IV) and aluminium(III) in aqueous solution. II. Formation constants for the monosilicate ions $SiO(OH)_3^-$ and $SiO_2(OH)_2^{2-}$. A precision study at 25 °C in a simplified seawater medium. Mar. Chem. 19, 521–532.

Takahashi, T., Olafsson, J., Goddard, J., Chipman, D.W., Sutherland, S.C., 1993. Seasonal variation of CO_2 and nutrients in the high-latitude surface oceans: A comparative study. Glob. Biogeochem. Cycles 7, 843–878.

Takahashi, T., Climatological mean and decadal changes in surface ocean pCO_2, and net sea-air CO_2 flux over the global oceans. Deep-Sea Res. II 554–577. http://dx.doi.org/10.1016/j.dsr2.2008.12.009.

Takahashi, T., Sutherland, S.C., Kozyr, A., 2013. Global Ocean Surface Water Partial Pressure of CO_2 Database: Measurements Performed During 1957–2012 (Version 2012). ORNL/CDIAC-160, NDP-088(V2012). Carbon Dioxide Information Analysis Center, Oak Ridge National Laboratory, U.S. Department of Energy, Oak Ridge, Tennessee. http://dx.doi.org/10.3334/CDIAC/OTG.NDP088(V2012).

Tanhua, T., et al., 2009. CARINA Data Synthesis Project. ORNL/CDIAC-157, NDP-091. Oak Ridge National Laboratory, U. S. Department of Energy, p. 11.

Walsh, J.J., et al., 1989. Carbon and nitrogen cycling within the Bering/Chukchi Seas: Source regions for organic matter effecting AOU demands of the Arctic Ocean. Prog. Oceanogr. 22, 277–359.

Weiss, R.F., 1974. Carbon dioxide in water and seawater: The solubility of a non-ideal gas. Mar. Chem. 2, 203–215.

Woodgate, R.A., Aagaard, K., Weingartner, T.J., 2006. Interannual changes in the Bering Strait fluxes of volume, heat and freshwater between 1991 and 2004. Geophys. Res. Lett. 33 (L15609), 2006. http://dx.doi.org/10.1029/2006GL026931.